Chapter 1

Synthesis & Characterization of……..

a) Mono Lacunary Phosphotungstate Anchored to MCM-41 (PW_{11}/MCM-41)

b) 12-Tungstophosphoric acid Anchored to MCM-48 (PW_{12}/MCM-48) & Mono Lacunary Phosphotungstate Anchored to MCM-48 (PW_{11}/MCM-48)

CHAPTER 1a

Mono Lacunary Phosphotungstate Anchored to MCM-41 (PW_{11}/MCM-41)

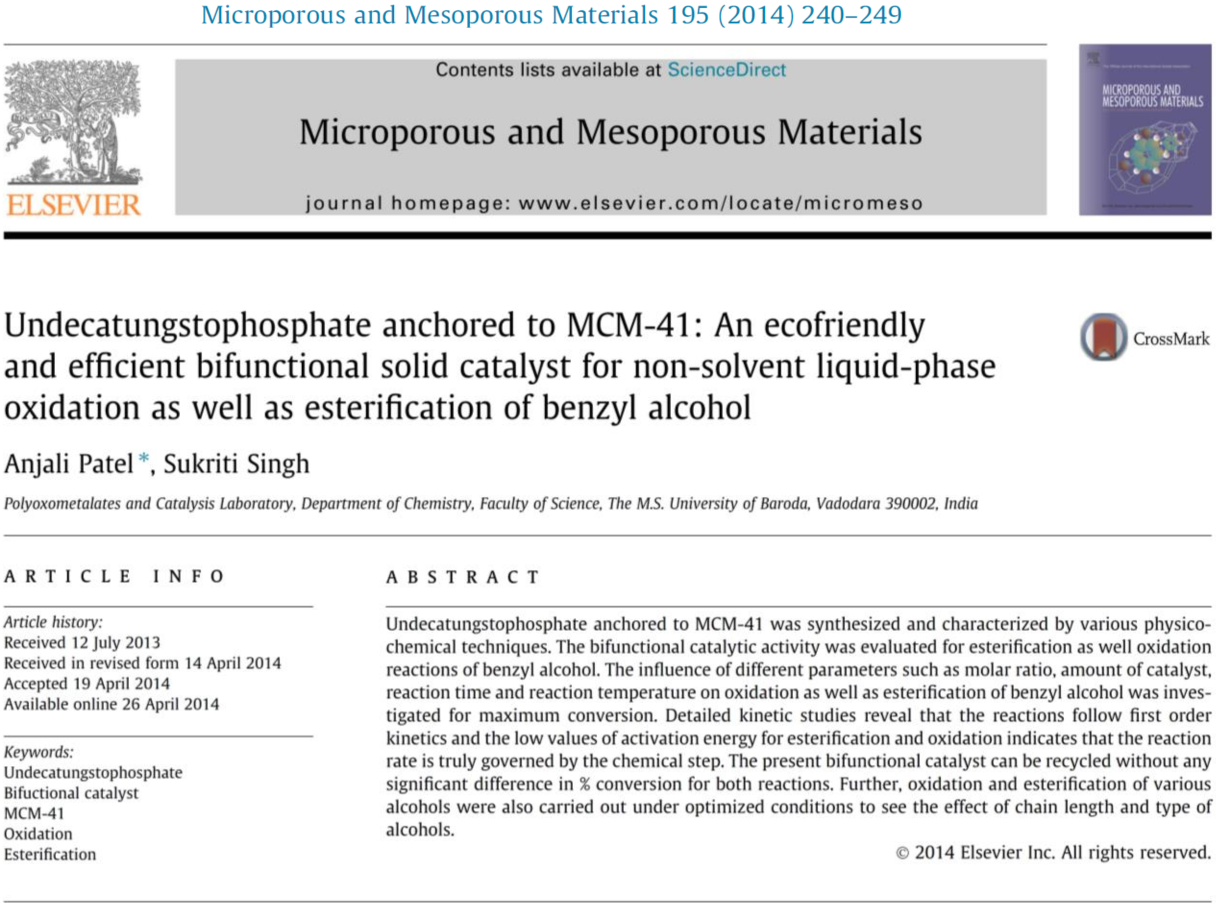

Microporous and Mesoporous Materials 195 (2014) 240–249

Contents lists available at ScienceDirect

Microporous and Mesoporous Materials

journal homepage: www.elsevier.com/locate/micromeso

Undecatungstophosphate anchored to MCM-41: An ecofriendly and efficient bifunctional solid catalyst for non-solvent liquid-phase oxidation as well as esterification of benzyl alcohol

Anjali Patel *, Sukriti Singh

Polyoxometalates and Catalysis Laboratory, Department of Chemistry, Faculty of Science, The M.S. University of Baroda, Vadodara 390002, India

ARTICLE INFO

Article history:
Received 12 July 2013
Received in revised form 14 April 2014
Accepted 19 April 2014
Available online 26 April 2014

Keywords:
Undecatungstophosphate
Bifuctional catalyst
MCM-41
Oxidation
Esterification

ABSTRACT

Undecatungstophosphate anchored to MCM-41 was synthesized and characterized by various physico-chemical techniques. The bifunctional catalytic activity was evaluated for esterification as well oxidation reactions of benzyl alcohol. The influence of different parameters such as molar ratio, amount of catalyst, reaction time and reaction temperature on oxidation as well as esterification of benzyl alcohol was investigated for maximum conversion. Detailed kinetic studies reveal that the reactions follow first order kinetics and the low values of activation energy for esterification and oxidation indicates that the reaction rate is truly governed by the chemical step. The present bifunctional catalyst can be recycled without any significant difference in % conversion for both reactions. Further, oxidation and esterification of various alcohols were also carried out under optimized conditions to see the effect of chain length and type of alcohols.

EXPERIMENTAL

Materials

All chemicals used were of A. R. grade. 12-Tungstophosphoric acid (PW_{12}), Disodium hydrogen phosphate (Na_2HPO_4), Sodium tungstate dihydrate ($Na_2WO_4 \cdot 2H_2O$), acetone, sodium hydroxide, Cetyl trimethyl ammonium bromide (CTAB) and Tetraethyl orthosilicate (TEOS) were used as received from Merck.

Synthesis of Na salt of Mono Lacunary Phosphotungstate (PW_{11}):

The mono lacunary phosphotungstate was synthesized by method as reported by Brevard et al. [1]. Sodium tungstate dihydrate (0.22 mol, 72.5 g) and anhydrous disodium hydrogen phosphate (0.02 mol, 2.84 g) were dissolved in 150-200 mL of distilled water. The solution was heated to 80-90 °C and pH adjusted to 4.8 with concentrated nitric acid (Scheme 1). The volume was then reduced to half by evaporation and the heteropolyanion separated by liquid-liquid extraction with 80-100 mL of acetone. The extraction was repeated until the acetone extract shows absence of nitrate ions. The extracted solid was dried in air. The obtained sodium salt of mono lacunary phosphotungstate was designated as PW_{11}.

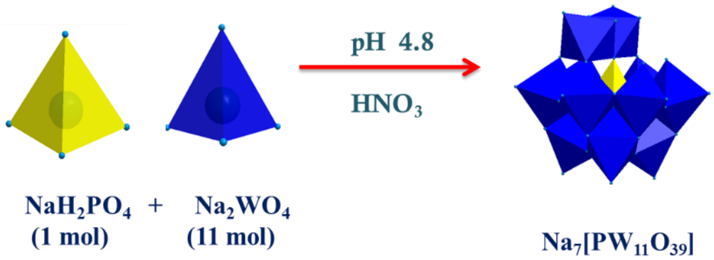

Scheme 1. Synthesis of mono-lacunary phosphotungstate from individual salts.

Synthesis of MCM-41

Synthesis of MCM-41 was carried out by following non-hydrothermal procedure reported by Q. Cai et al. [2] with slight modification. Surfactant (CTAB) was added to a dilute solution of NaOH (2 M, 3.5 mL NaOH in 480 mL distilled water) with stirring at 60 °C. After the solution became clear, TEOS (5 mL) was added drop wise and obtained gel was aged for 2 h at 60 °C. The resulting product was filtered, washed with distilled water and dried at room temperature. The obtained solid was calcined at 555 °C in air for 5 h and designated as MCM-41. A schematic representation for synthesis of MCM-41 is shown in Figure 1.

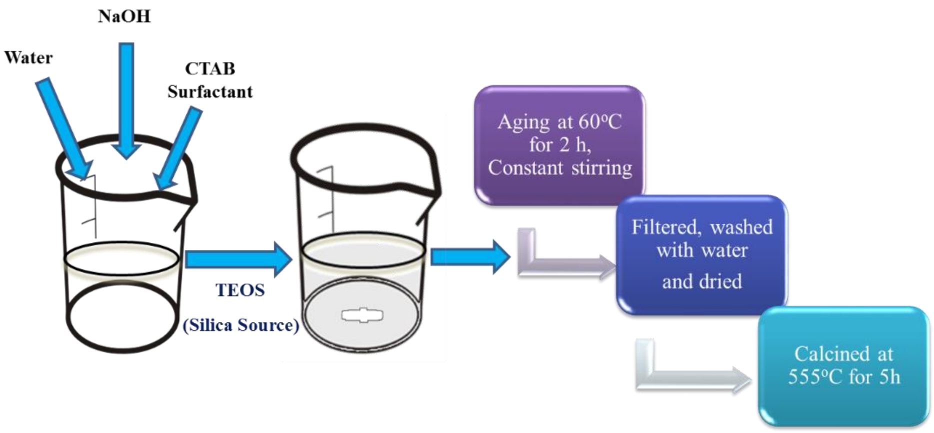

Figure 1. Synthesis scheme for MCM-41 under non-hydrothermal conditions.

Synthesis of the catalysts

PW_{12} anchored to MCM-41 [3]

PW_{12} was anchored to MCM-41 by impregnation method. 1 g of MCM-41 was impregnated with an aqueous solution of PW_{12} (0.1g/10 mL of distilled water). The water from the suspension was allowed to evaporate at 100 °C in an oven. Then the resulting mixture was dried at 100 °C with stirring for 10 h. The material thus obtained was designated as $(PW_{12})_1$/MCM-41. Same procedure was followed for the synthesis of a series of PW_{12} anchored catalyst (0.2-0.4 g/20-40 mL of distilled water). The obtained materials with different loading were designated as $(PW_{12})_2$/MCM-41, $(PW_{12})_3$/MCM-41 and $(PW_{12})_4$/MCM-41, respectively.

PW_{11} anchored to MCM-41

PW_{11} was anchored to MCM-41 by impregnation method. 1 g of MCM-41 was impregnated with an aqueous solution of PW_{11} (0.1g/10 mL of distilled water). The water from the suspension was allowed to evaporate at 100 °C in an oven. Then the mixture was dried at 100 °C with stirring for 10 h. The obtained material was treated with 0.1 N HCl, filtered, washed with distilled water and dried at 100 °C. The material thus obtained was designated as $(PW_{11})_1$/MCM-41. Same procedure was followed for the synthesis of a series of PW_{11} anchored catalyst (0.2-0.4 g/20-40 mL of distilled water). The obtained materials with different loadings were designated as $(PW_{11})_2$/MCM-41, $(PW_{11})_3$/MCM-41 and $(PW_{11})_4$/MCM-41, respectively.

CHARACTERIZATION

Characterization is a central aspect of catalyst development [4-6]. The elucidation of the structures, compositions, and chemical properties of both the supports used in heterogeneous catalysis as well as the active species present on the surfaces of the supported catalysts is very important for a better understanding of the relationship between catalyst properties and catalytic performance [6]. The basic information on the structure-catalytic property relationship for catalyst systems will ultimately be of value in the design of new efficient catalysts [7]. A representative diagram describing the correlation between the active species and the support is shown in Scheme 2.

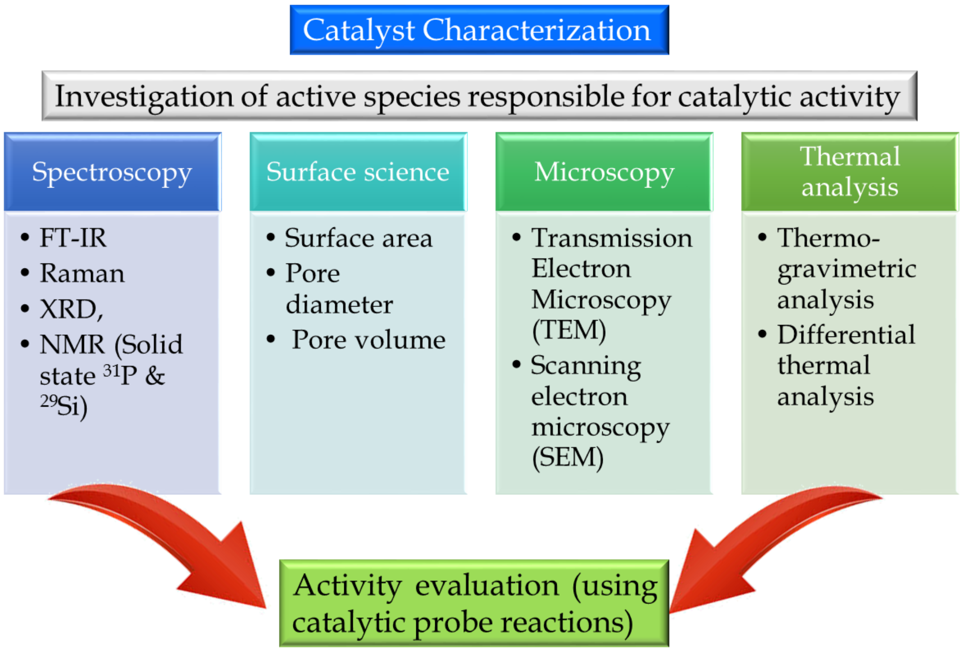

Scheme 2. Block diagram of various techniques used in characterization of catalyst.

In the present work the following techniques have been used for the characterization.

BET measurement were carried out on Micromeritics Surface area Analyzer (Model: ASAP 2020) at -196 °C. From the adsorption desorption isotherms specific surface area was calculated using Brunauer-Emmett-Teller (BET) method. The samples were degassed under vacuum (5-10.3 mmHg) at 150 °C for 4 h, prior to measurement, to evacuate the physisorbed moisture. Further the pore size distributions were calculated applying the Barrett-Joyner-Halenda (BJH) method to the desorption branches of the isotherm.

Elemental Analysis: Energy-dispersive X-ray spectroscopy (EDS or EDX) was carried out using JSM 5610 LV combined with INCA instrument for EDX-SEM analyzer for the quantitative identification of metal ions.

Thermo Gravimetric- Differential thermal analysis (TGA-DTA) measurements were carried out on the Mettler Toledo Star SW 7.01 in the temperature range 40 °C to 600 °C. All measurements were carried out under nitrogen atmosphere with a flow rate of 2 mL/ min and heating rate of 10 °C/ min.

Fourier Transform- Infrared Spectroscopy (FT-IR) were recorded on FT-IR Perkin Elmer instrument at room temperature using KBr pellets in the range of 4000 cm^{-1} to 400 cm^{-1}. The powdered samples were ground with KBr in 1: 10 ratio and pressed (5 ton/cm^2) for making the pellets. The data were collected at an average of 25 scans.

Raman spectra were recorded on a FT-Raman Spectrophotometer Model Bruker FRA 106 with resolution- 2 cm^{-1} and number of scans- 4.

Solid state magic- angle spinning (MAS)- NMR (^{31}P and ^{29}Si) was carried out on a BRUKER Avance DSX-300 MHz spectrometer under ambient conditions. ^{29}Si NMR spectrometer were recorded at 121.49 MHz using a 7 mm rotor probe with TMS as an external standard. The spinning rate was 5-7 kHz (Number of scans- 1024), number of acquisitions AQ: 0.0048888 Sec. For ^{31}P MAS NMR, 85% H_3PO_4 was used as an external standard and number of scans- 9216.

Powder X-Ray Diffraction (XRD) pattern were obtained using the instrument Philips Diffractometer (Model PW-1830) with Cu Kα radiation (1.5417 Å) and scanning angle from 0° to 60°.

Scanning Electron Microscopy (SEM) were studied using JEOL SEM instrument (Model- JSM-5610 LV) with scanning electron electrode at 15 kV. Scanning was done at 1 mm range and images were taken at various magnifications.

Transmission Electron Microscopy (TEM) was carried out on JEOL (JAPAN) TEM instrument (model-JEM 100CX II) with accelerating voltage 220 kV. The samples were dispersed in ethanol and ultra-sonicated for 5-10 minutes. A small drop of the sample was then taken in a carbon coated copper grid and dried before viewing.

Acidity measurement

A small quantity (0.1 mL) of 0.05 N, n-butylamine in acetonitrile was added to a suspension of 0.5 g of the catalyst in 50 mL of acetonitrile and the system was stirred at 25 ^{o}C. Then, the suspension was potentiometrically titrated against 0.05 N, n-butylamine in acetonitrile. The electrode potential variation was measured with a digital pH meter.

The acidity of the catalyst measured by this technique allows us to evaluate the total number of acid sites as well as their acidic strength. In order to interpret the results, it is suggested that the initial electrode potential (Ei) indicates the maximum acid strength of the surface sites and the range where the plateau is reached (meq/g solid) indicates the total number of acid sites [8].

RESULTS AND DISCUSSION

Characterization of PW_{12}

PW_{12} was characterized by various physicochemical techniques in our previous publication [3].

Characterization of PW_{11}

The PW_{11} was isolated as sodium salt after completion of reaction and the remaining solution was filtered off. The filtrate was analysed to estimate the amount of non-reacted W [9]. The observed % of W in the filtrate was 0.5%, which corresponds to loss of one equivalent of tungsten from $H_3PW_{12}O_{40}.nH_2O$. The observed values for elemental analysis are in good agreement with the theoretical values indicating formation of PW_{11}. Analytically calculated (%): Na- 5.4, W- 65.2, P- 0.99, O- 27.5; Found (%): Na- 5.2, W- 65.8, P- 1.01, O- 27.9.

The **TGA** of PW_{11} shows 8% (Figure 2) weight loss in the temperature range 100–150 °C due to loss of crystalline water. It also shows 2% weight loss up to 400 °C which may be due to the decomposition of the Keggin structure. The DTA of PW_{11} (Figure 2) shows an endothermic peak at 160 °C indicating the loss of crystallization water molecules. Further it shows an exothermic peak at 450 °C which may be due to some phase change or decomposition of the lacunary Keggin ion.

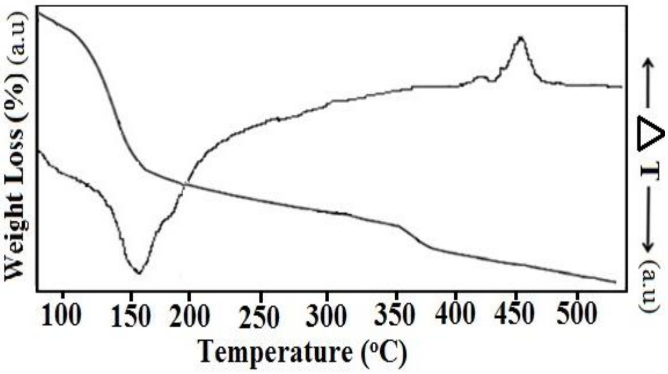

Figure 2. TG-DTA thermogram of PW_{11}.

Number of water molecules was determined from the TGA curve using the following formula,

$$18\ n = \left(\frac{X\ [M + 18\ n]}{100}\right)$$

Where, n = number of water molecules, X = % loss from TGA and M = molecular weight of substance (without water of crystallization)

Based on the elemental as well as TGA data the chemical formula of the isolated sodium salt was proposed as **$Na_7[PW_{11}O_{39}].13H_2O$.**

The **FT-IR** spectra for PW_{12} and PW_{11} are shown in Figure 3. In the FT-IR, P-O stretching band (1080 cm^{-1}) for PW_{12} splits into two new bands at 1085 and 1043 cm^{-1} in PW_{11}. This is due to the loss of one W-O unit and lowering of the symmetry from Td (PW_{12}) to Cs (PW_{11}) around the central heteroatom, phosphorus. Apart from that, two W-O-W frequencies at 808, 863 cm^{-1} and one W=O stretching frequency at 952 cm^{-1} was observed [10-11].

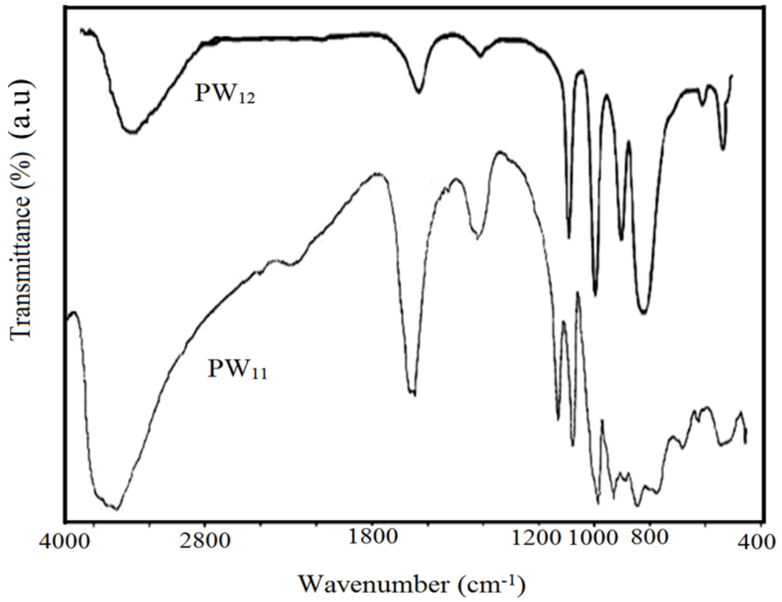

Figure 3. FT-IR spectrum for PW_{12} and PW_{11}

Raman spectra of PW_{12} show bands at 1010, 990, 900, 550, and 217 cm^{-1}, corresponding to ν_s (W=O_d), ν_{as} (W-O_d), ν_{as} (W-O_b-W), ν_s (W-O_c-W), and ν_s (W-O_a), respectively (Figure 4), where O_a, O_b, O_c, and O_d are the oxygen atoms linked to phosphorous, oxygen atoms bridging two tungsten (from two different triads for O_b and from the same triad for O_c), and to the terminal oxygen W=O, respectively [12]. Raman spectra of PW_{11} show bands at 990, 985, 909, 513, and 225 cm^{-1}, (Figure 4) corresponding to v_s ($W=O_d$), v_{as} ($W-O_d$), v_{as} ($W-O_b-W$), v_s ($W-O_c-W$), and v_s ($W-O_a$), respectively, which confirms the formation of lacunary species.

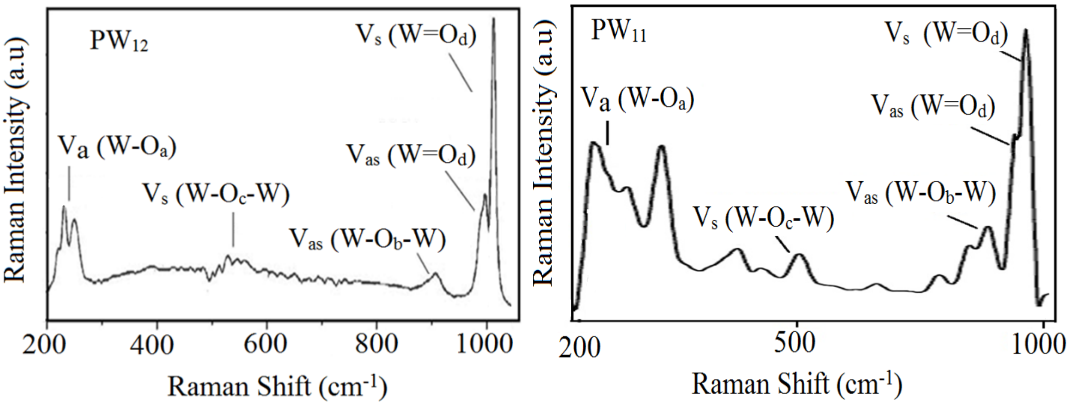

Figure 4. FT-Raman spectra of PW_{12} and PW_{11}.

The **^{31}P NMR** chemical shift provides important information concerning the chemical environment around phosphorous. It is well known that the removal of one WO from PW_{12} Keggin unit leads to decrease in the δ value by 4.5 ppm (δ for PW_{12} -15.6 ppm and for PW_{11} -11.3 ppm) [12]. MAS NMR spectrum of PW_{11} shows an intense peak at -11.30 ppm (Figure 5), indicating formation of mono-lacunary species as confirmed by literature report [12].

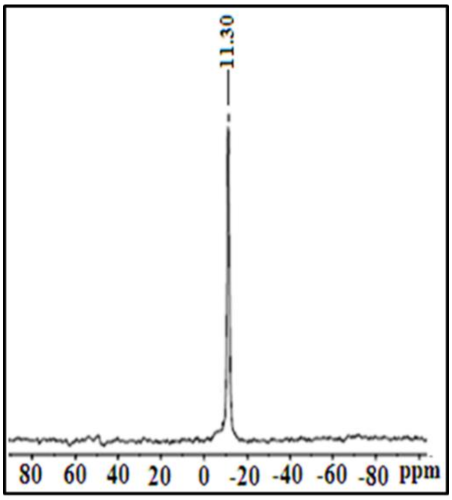

Figure 5. ^{31}P MAS NMR spectra of PW_{11}.

Thus, the thermal as well as spectral studies confirm the formation of PW_{11}.

Characterization of PW_{12}/MCM-41 [3] as well as PW_{11} /MCM-41

A detailed study on the characterizations of $(PW_{12})_3$*/MCM-41 has already been carried out by our group earlier [3]. However in the present thesis BET, EDS, TG-DTA, FT-IR, and* ^{31}P *MAS NMR are given for comparison purpose.*

Leaching Test

Leaching is a negative property for any catalyst. Any leaching of catalyst from the support would make the catalyst unattractive. So, it is necessary to study the stability of polyanion onto support in order to reuse the catalyst. When the polyoxometalate react with a mild reducing agent such as ascorbic acid [13], it develops blue coloration, which can be used for the quantitative characterization for the leaching of polyoxometalate from the support. In the current work, we have used this method for determining the leaching of PW_{12}/PW_{11} from MCM-41 as well as MCM-48 supports.

Standard samples amounting to 1-5% of PW_{12}/PW_{11} in water were prepared. To 10 mL of the above samples, 1 mL of 10% ascorbic acid was added. The mixture was diluted to 25 mL. The resultant solution was scanned at a λ_{max} of 785 nm for its absorbance values. A standard calibration curve was obtained by plotting values of absorbance with percentage solution. In a typical reaction, 1 g catalyst was refluxed for 4 h with 10 mL of conductivity water. 1 mL of the supernatant solution was then treated with 10% ascorbic acid. No development of blue color indicates absence of any leaching. The same procedure was repeated with water, methanol, glycerol and also with the filtrates of all the reaction mixtures after completion of the reaction. The above procedure was followed for all catalysts and no leaching was found. For each case, absence of blue color indicates no leaching of PW_{12}/PW_{11} from support into reaction medium. The study indicates the presence of chemical interaction between the PW_{12}/PW_{11} and MCM-41/MCM-48, as well as stability of the resultant catalysts under reaction conditions.

The values of **BET surface area**, pore size and pore volumes of support and the catalysts are presented in Table 1. As the PW_{12}/PW_{11} loading increases the surface area, pore diameter and pore volume all strongly decrease relative to the support indicating high dispersion of active species inside the pores of support. The decrease in surface area of catalysts was the first evidence of chemical interaction between PW_{12}/PW_{11} and MCM-41. Further, up to 30% loading constant decrease in the surface area was observed which may be due to the monolayer formation of the active species. This confirms that the active species are located inside the channels of MCM-41. Further increase in % loading to 40%, leads to drastic decrease in the surface area of $(PW_{12})_4$/MCM-41 and $(PW_{11})_4$/MCM-41, which may be due to the surface saturation as well as blocking of the pores by active species. Hence, 30% loaded catalysts, $(PW_{12})_3$/MCM-41 and $(PW_{11})_3$/MCM-41, were selected for the further detailed characterization.

Table 1. Textural properties of support and catalysts.

Materials	Surface area (m^2/g)	Pore diameter (Å)	Pore Volume (cm^3/g)
MCM-41	659	47.9	0.79
$(PW_{12})_1$/MCM-41	400	30.69	0.55
$(PW_{12})_2$/MCM-41	372	30.53	0.50
$(PW_{12})_3$/MCM-41	360	30.13	0.50
$(PW_{12})_4$/MCM-41	139	11.1	0.33
$(PW_{11})_1$/MCM-41	352	35.2	0.54
$(PW_{11})_2$/MCM-41	305	31.5	0.45
$(PW_{11})_3$/MCM-41	252	30.1	0.42
$(PW_{11})_4$/MCM-41	119	15.5	0.10

Nitrogen adsorption-desorption isotherms and BET pore size distribution curves for MCM-41, $(PW_{12})_3$/MCM-41 and $(PW_{11})_3$/MCM-41 (Figure 6) present the Type IV isotherm pattern, according to the IUPAC classification and exhibited an H1 hysteresis loop which is a characteristic of mesoporous solids [14]. The adsorption branch of each isotherms showed a sharp inflection, which means a typical capillary condensation within uniform pores. The position of the inflection point is clearly related to the diameter of the mesopore, and the sharpness of this step indicates the uniformity of the mesopore size distribution. The pore size distributions (Figure 6a, b, c) in the inset show that all the samples have narrow pore size distribution within the mesopore range.

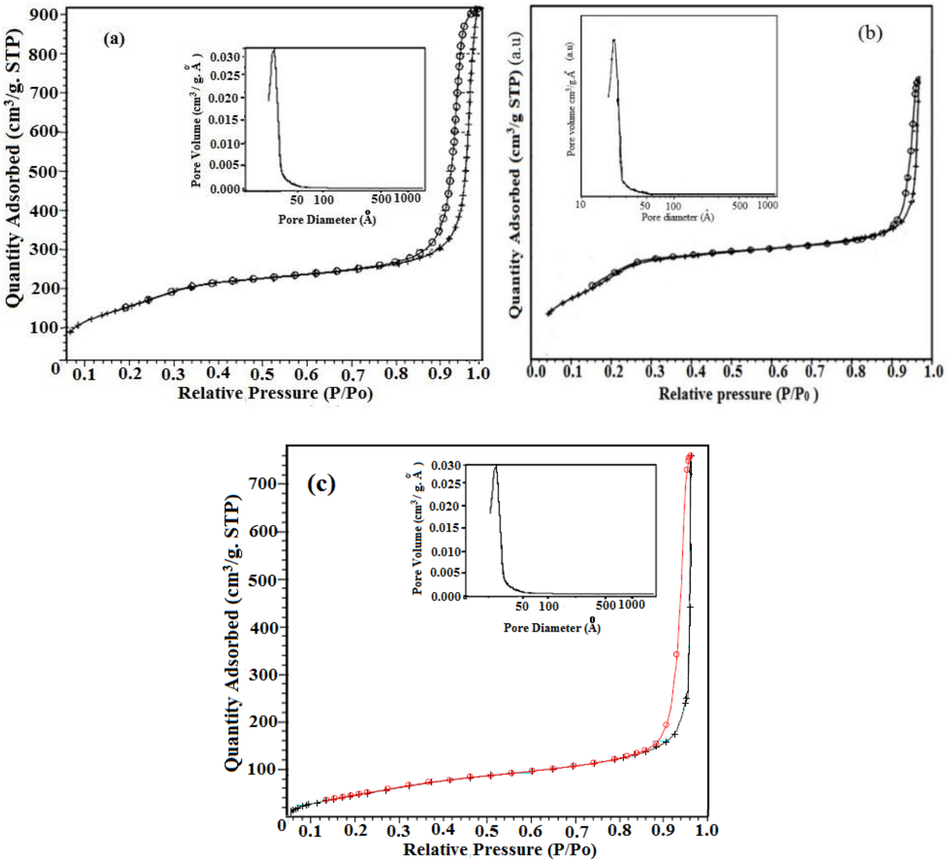

Figure 6. Nitrogen adsorption - desorption isotherm and pore size distribution of (a) MCM-41, (b) (PW$_{12}$)$_3$/MCM-41 and (c) (PW$_{11}$)$_3$/MCM-41.

The **EDS elemental analysis** for $(PW_{12})_3$/MCM-41 and $(PW_{11})_3$/MCM-41 is shown in Table 2. The results obtained from EDS were in good agreement with the analytically calculated values.

Table 2. EDS elemental analysis.

Catalyst	Elemental analysis (weight %)					
	O	Si	W		P	
			By EDS	Theoretical	By EDS	Theoretical
$(PW_{12})_3$/MCM-41	53.9	27.8	18.0	19.0	0.30	0.32
$(PW_{11})_3$/MCM-41	52.7	30.8	16.2	16.5	0.18	0.19

TG-DTA of PW_{12} is shown in Figure 7. The unsupported pure PW_{12} exhibits weight loss in three stages at 100, 200 and 485 ^oC as indicated by the TGA curve (Figure 7a). These can be attributed to initial weight due to adsorbed water, second weight loss due to loss of water of crystallization near 200 ^oC to give the Keggin structure, which is stable on heating up to 350 ^oC. The endothermic peak observed on DTA curve at 485 ^oC may be attributed to the decomposition of the Keggin structure of PW_{12} into the simple oxides [15]. TGA of MCM-41 (Figure 7c) showed initial weight loss of 6.14% at 100 ^oC. This is due to the loss of adsorbed water molecules. The final 7.92% weight loss above 450 ^oC is due to the condensation of silanol groups to form siloxane bonds. After that absence of any weight loss indicates that support is stable up to 600 ^oC.

The TGA of $(PW_{12})_3$/MCM-41 (Figure 7b) shows initial weight loss of 3.6% due to the loss of adsorbed water. Second weight loss of 1.2% between 150-250 ^oC corresponds to the loss of water of crystallization of Keggin ion. After that another gradual weight loss was also observed from 250-500 ^oC due to the difficulty in removal of water contained in PW_{12} molecules inside the channels of MCM-41. This type of inclusion causes the stabilization of PW_{12} molecules inside the channels of MCM-41.

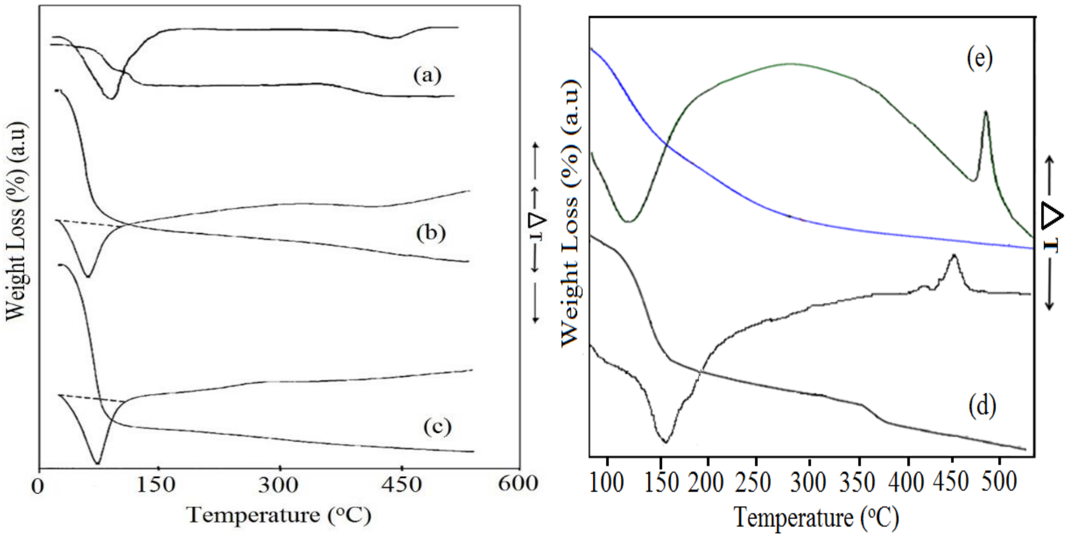

Figure 7. TG-DTA profiles of (a) PW_{12}, (b) $(PW_{12})_3$/MCM-41, (c) MCM-41, (d) PW_{11}, and (e) $(PW_{11})_3$/MCM-41.

The TGA of PW_{11} shows 8% weight loss in the temperature range 100-150 °C due to the loss of crystalline water (Figure 7d). Further, 2% weight loss was observed at 400 °C. Also DTA studies show an Endothermic peak at 160 °C, due to loss of water of crystallization and exothermic peak at 450 °C is due to decomposition of the lacunary structure. The TGA of $(PW_{11})_3$/MCM-41 showed an initial weight loss of 3.6% due to the loss of adsorbed water (Figure 7e). Second weight loss of 1.2% between 150 and 250 °C corresponds to the loss of water of crystallization of lacunary PW_{11} ion. Further, it does not show any weight loss up to 500 °C, indicating the synthesized catalyst is stable up to 500 °C. The DTA studies show an increase in the stability of PW_{11} after being supported on MCM-41 as there is a shift in exothermic peak to 500 °C.

FT-IR spectra of MCM-41, PW_{12}, and $(PW_{12})_3$/MCM-41 are shown in Figure 8. The FT-IR spectra of MCM-41 (Figure 8a, Left) shows a broad band around 1300-1000 cm^{-1} corresponding to asymmetric stretching of Si-O-Si. The band at 801 and 458 cm^{-1} are due to symmetric stretching and bending vibration of Si-O-Si, respectively. The band at 966 cm^{-1} corresponds to symmetric stretching vibration of Si-OH. FT-IR spectra of $(PW_{12})_3$/MCM-41 (Figure 8b, Left) is almost same as that of MCM-41. The reported bands for PW_{12}, at 1088 cm^{-1}, 987 cm^{-1} and 800 cm^{-1} corresponding to W-O-W bending, W-O and P-O symmetric stretching respectively [16], are absent in $(PW_{12})_3$/MCM-41 may be due to overlapping with the bands of support.

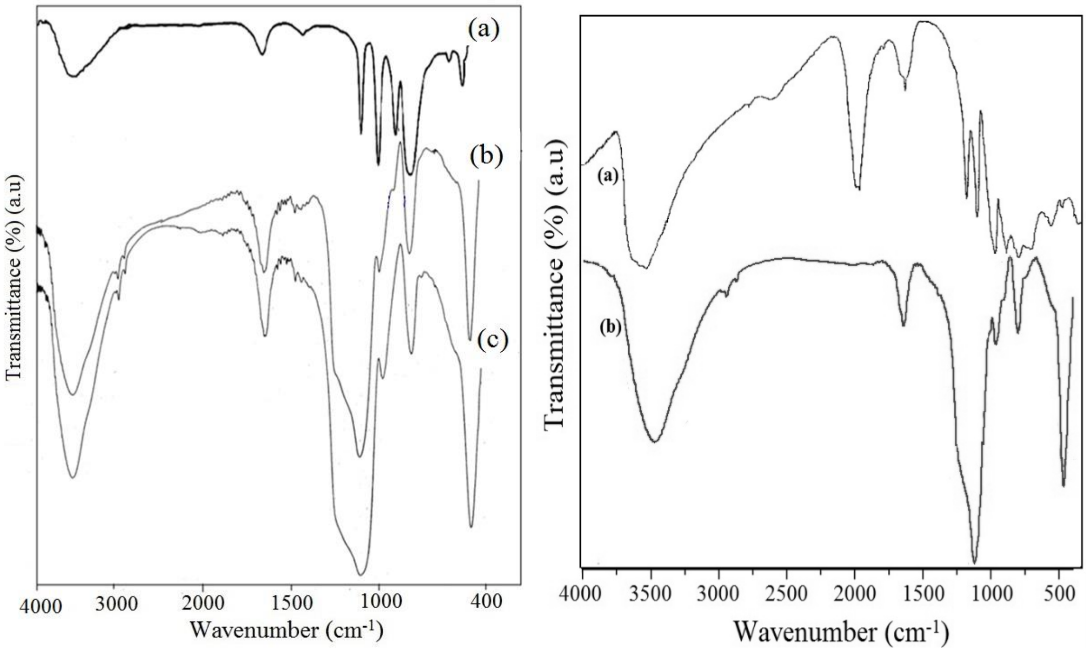

Figure 8. FT-IR spectra of Left- (a) MCM-41, (b) $(PW_{12})_3$/MCM-41 and (c) PW_{12}; Right- (a) PW_{11} and (b) $(PW_{11})_3$/MCM-41.

In FT-IR of PW_{11} (Figure 8a, Right), P-O stretching band splits into two new bands at 1085 and 1043 cm^{-1}. This is due to loss of one W=O unit and lowering of symmetry from T_d (PW_{12}) to Cs (PW_{11}) around the central heteroatom, phosphorus [16]. Apart from that the W-O-W and W=O stretching bands appear at 808, 863 and 952 cm^{-1} respectively. The reported bands for PW_{11}, at 1085, 1043, 808 cm^{-1} corresponding to P-O, W-O-W, respectively, are absent in $(PW_{11})_3$/MCM-41 due to overlapping with the bands of MCM-41 (Figure 8b, Right). Also bands of PW_{11} at 952 and 863 cm^{-1} attributed to W=O and W-O-W, respectively shifts to a higher wave number (962 and 896 cm^{-1}) in $(PW_{11})_3$/MCM-41, indicating strong interaction between the lacunary Keggin anion and silanol groups of the support.

Raman spectra of PW_{11} and $(PW_{11})_3$/MCM-41 are shown in Figure 9. Raman spectra of PW_{11} show bands at 990, 985, 909, 513, and 225 cm^{-1}, corresponding to v_s (W=O_d), v_{as} (W-O_d), v_{as} (W-O_b-W), v_s (W-O_c-W), and v_s (W-O_a), respectively (Figure 9a) [11]. The spectra for $(PW_{11})_3$/MCM-41 (Figure 9b) shows bands at 987, 912, 520 and 216 cm^{-1} corresponding to v_{as} (W=O_d), v_{as} (W-O_b-W), v_s (W-O_c-W), and v_s (W-O_a), respectively, except v_{as} (W=O_d) band. The presence of all reported bands of lacunary PW_{11} in catalyst indicates that the structure of PW_{11} is intact even after anchoring. Furthermore, slight shift in the Raman bands in catalyst indicates chemical interaction of active species PW_{11} with the surface silanol groups of MCM-41.

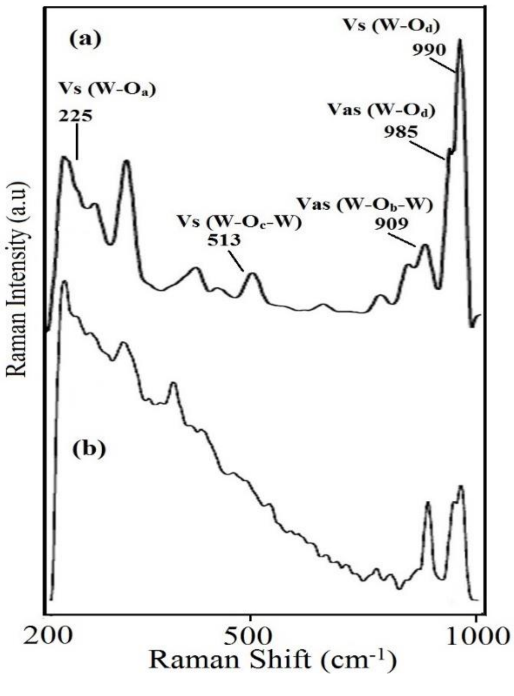

Figure 9. Raman spectra of (a) PW_{11} and (b) $(PW_{11})_3$/MCM-41.

^{31}P MAS NMR spectra of PW_{12}, and $(PW_{12})_3$/MCM-41 are shown in Figure 10a, b. The pure PW_{12} shows single peak at -15.62 ppm and is in good agreement with the reported one [16]. The ^{31}P NMR spectrum of $(PW_{12})_3$/MCM-41 shows single peak at -15.28 ppm. No appreciable change in chemical shift value indicates retained of PW_{12} after anchoring to MCM-41. ^{31}P MAS NMR spectrum for PW_{11} shows an intense peak at -11.30 ppm (Figure 10c), indicating the formation of the mono-lacunary species as confirmed by literature report [17].

The ^{31}P MAS NMR for the $(PW_{11})_3$/MCM-41 (Figure 10d) reveals three resonances at -2.9 ppm, -8.4 ppm and -12.7 ppm. The peak at -2.9 ppm reveals the presence of strongly adsorbed highly fragmented Keggin unit.

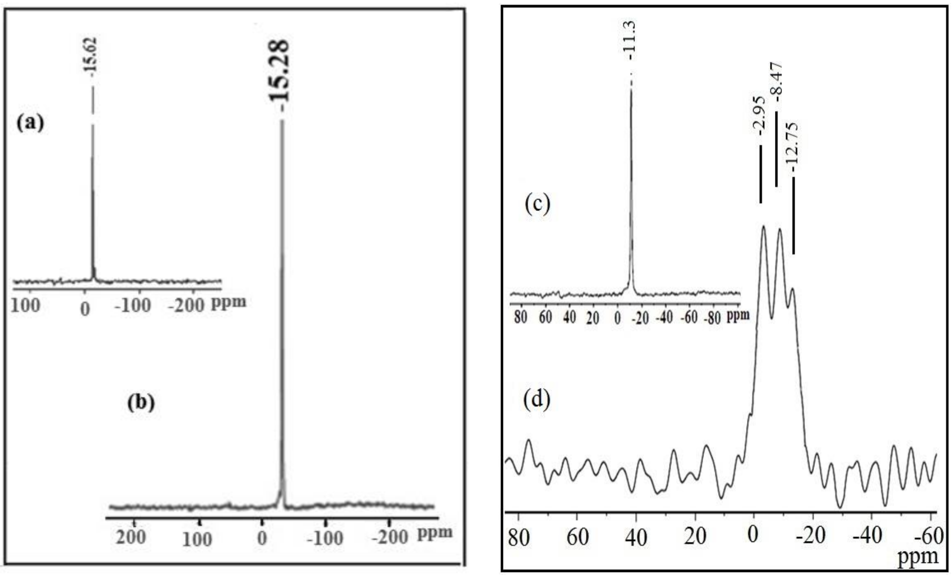

Figure 10. ^{31}P MAS NMR spectra of (a) PW_{12}, (b) $(PW_{12})_3$/MCM-41, (c) PW_{11}, and (d) $(PW_{11})_3$/MCM-41.

The peak at -8.4 ppm indicates the presence of phosphate character due to the partial fragmentation of the Keggin unit to produce, "11-defect" Keggin species and the peak at -12.7 ppm is due to intact Keggin PW_{11} unit interacting with surface hydroxyl groups of the support. The slight broadening and shifting in the peak may be due to interaction of PW_{11} and MCM-41. This observation is in agreement with the related values reported by Edwards *et al*. [17] and indicates that the active species PW_{11} is present in the fragmented form and is not decomposed.

^{29}Si MAS-NMR is the most important method to study chemical environment around the silicon nuclei in mesoporous silica materials and concentration of the silanol groups. ^{29}Si MAS NMR of MCM-41 show signals with chemical shifts at -93, -103 and -110 ppm resulting from Q^2, Q^3 and Q^4 silicon nuclei, respectively (Figure 11a). Here Q^n resembles to a silicon with n siloxane linkages, i.e., Q^2 to $Si(O\text{-}Si)_2(O\text{-}X)_2$, where X is H or PW_{11} , Q^3 to $(X\text{-}O)Si(O\text{-}Si)_3$

and Q^4 to $Si(O\text{-}Si)_4$ [18]. The significant shift in the chemical shift (Figure 11b, Table 3) arises from strong hydrogen bonding between PW_{11} and Q^2 (surface silanol groups) (δ -99 ppm) of MCM-41. The presence of resonance originating from Q^3 (δ -100 ppm) and Q^4 (δ -109.6 ppm) in the catalyst indicates that MCM-41 retains its structure (Figure 11b). In addition to this the intensity of Q^2, Q^3 peaks decreases in catalyst and Q^4 peak at (δ -109.6 ppm) remains intact which suggests that there is interaction of PW_{11} with MCM-41 and the mesoporous structure of MCM-41 was intact even after anchoring.

Table 3. ^{29}Si chemical shifts of support and catalyst.

Material	Q^2 $Si(O\text{-}Si)_2(OH)_2$	Q^3 $Si(O\text{-}Si)_3(OH)$	Q^4 $Si(O\text{-}Si)_4$
MCM-41	-93	-103	-110
$(PW_{11})_3$/MCM-41	-99	-100	-109.6

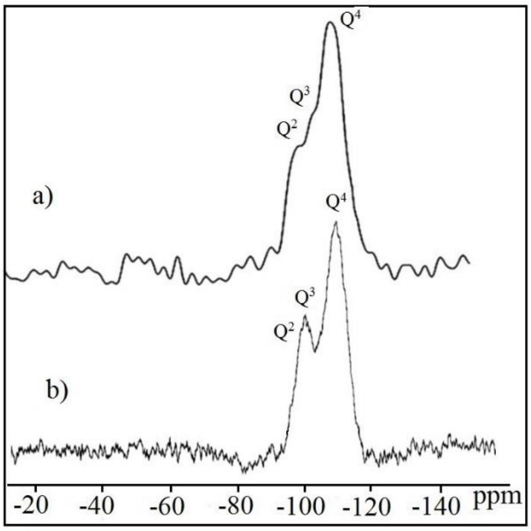

Figure 11. ^{29}Si MAS NMR spectra of (a) MCM-41 and (b) $(PW_{11})_3$/MCM-41.

To study the dispersion of PW_{11} species on the support, materials were further characterized by XRD, SEM and TEM.

The **low angle XRD** pattern of MCM-41 shows an intense diffraction peak at 2.43° and two peaks between 3.2- 4.8°, which are assigned to the lattice faces (100), (110) and (200), respectively, suggesting a well ordered channels of

MCM-41 (Figure 12b). The (100) peak in the case of catalyst is shifted to lower angles with broadening, indicating a lattice expansion during the incorporation and a decrease in the dimensions of the scattering domain [19]. No separate characteristic peaks of the crystalline phase of PW_{11} were observed in $(PW_{11})_3$/MCM-41 (Figure 12c), indicating fine dispersion of active species PW_{11} inside the hexagonal channels of MCM-41.

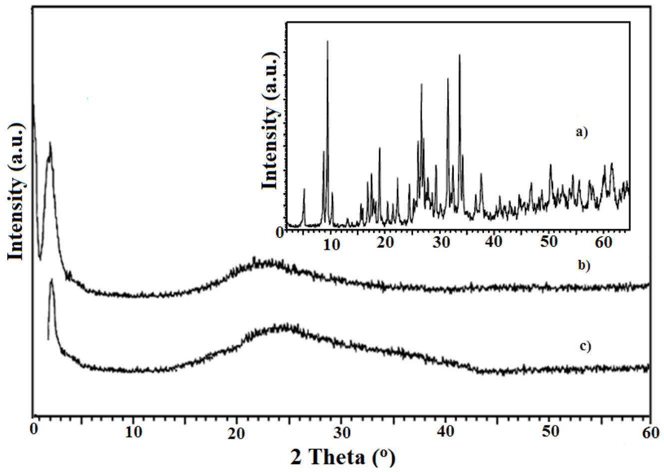

Figure 12. X-ray diffraction patterns of (a) PW_{11}, (b) MCM-41 and (c) $(PW_{11})_3$/MCM-41.

SEM images of support and the catalyst are shown in Figure 13. The surface morphology of $(PW_{11})_3$/MCM-41 was almost identical to that of MCM-41. No change in surface morphology of the catalyst and absence of separate crystallites of bulk phase PW_{11} in the catalyst, indicates that the PW_{11} species are well dispersed inside the channels of MCM-41.

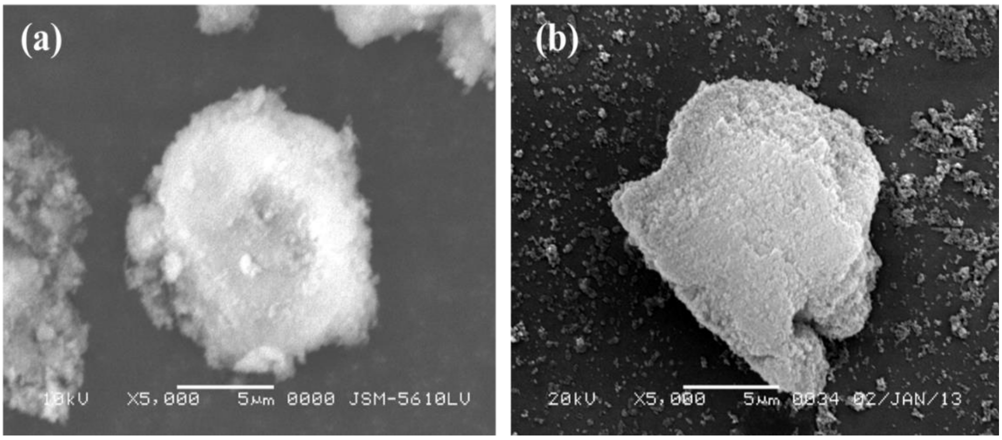

Figure 13. SEM images of (a) MCM-41 and (b) $(PW_{11})_3$/MCM-41.

TEM images of MCM-41 and $(PW_{11})_3$/MCM-41 at various magnifications are shown in Figure 14. The TEM images of MCM-41 (Figure 14 a, b) displays the morphology of hexagonal arrays of channels with uniform pore size, at 100 and 50 resolution. The TEM images of $(PW_{11})_3$/MCM-41 (Figure 14 c, d) shows that most of the pores are covered with fine particles of PW_{11}. The uniform distribution and lack of any agglomerates on the support agrees well with the XRD data. This indicates uniform dispersion of PW_{11} inside the hexagonal pores of MCM-41.

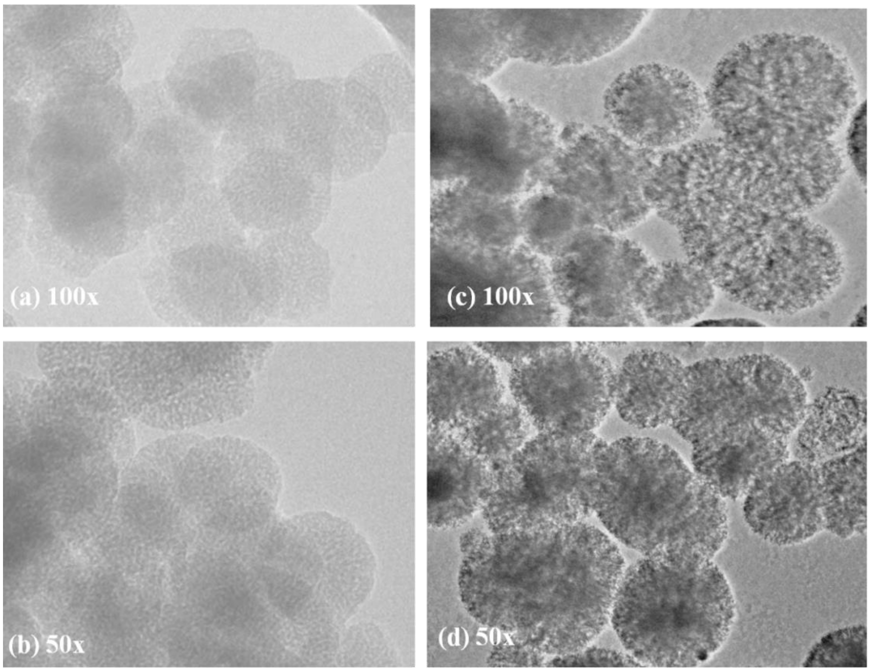

Figure 14. TEM images of (a, b) MCM-41 and (c, d) $(PW_{11})_3$/MCM-41.

BET measurement is the first indication of chemical interaction with the support. FT-IR, Raman spectra, ^{31}P MAS NMR and ^{29}Si MAS NMR shows that Keggin structure remains intact even after anchoring and there is strong interaction with MCM-41. XRD, SEM and TEM show fine dispersion of POMs inside the channels of MCM-41.

According to Vasquez et al [20], the **potentiometric titrations** with n-butylamine enable the quantitative determination of types of acid sites of the solid acid catalysts. The acidic strength of surface sites can be assigned according to the following ranges: very strong site, Ei > 100 mV; strong site, 0

< Ei < 100 mV; weak site, -100 < Ei < 0 mV and very weak site, Ei < -100 mV. The parent PW_{12} is well known to possess very good acidity, hence these properties are also retained the loaded catalysts, $(PW_{12})_3$/MCM-41 giving high total number of acidic sites (Table 4).

Table 4. Acidity properties of support and different loading of catalysts.

Material	Acidic strength Ei (mV)	Strength of acid sites (mequiv. g^{-1})		No. of acid sites in mequiv. g^{-1}
		Very strong	Strong	
MCM-41	48	0	2.0	2.0
$(PW_{12})_3$/MCM-41	410	1.9	1.5	3.6
$(PW_{11})_3$/MCM-41	250	1.0	1.5	3.0

The plots of electrode potential as a function of meq. n-butyl amine/g are shown in Figure 15. The range where the plateau is reached (meq/g solid) indicates the total number of acid sites (Table 4). It is clear from table, that on incorporation of PW_{12}/PW_{11} species the strength of acid sites of catalysts increases to a great extent. The acidic strength of $(PW_{11})_3$/MCM-41 is lower than that of $(PW_{12})_3$/MCM-41, this is due to the reason that removal of one tungsten-oxygen unit from the parent PW_{12} reduces the acidity of PW_{11}.

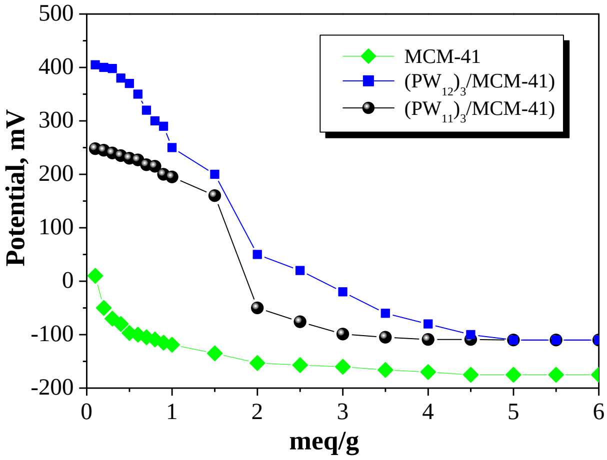

Figure 15. Potentiometric titration curves, MCM-41, $(PW_{12})_3$/MCM-41 and $(PW_{11})_3$/MCM-41.

CHAPTER 1b

1) 12-tungstophosphoric acid Anchored to MCM-48 (PW_{12}/MCM-48)
2) Mono Lacunary Phosphotungstate Anchored to MCM-48 (PW_{11}/MCM-48)

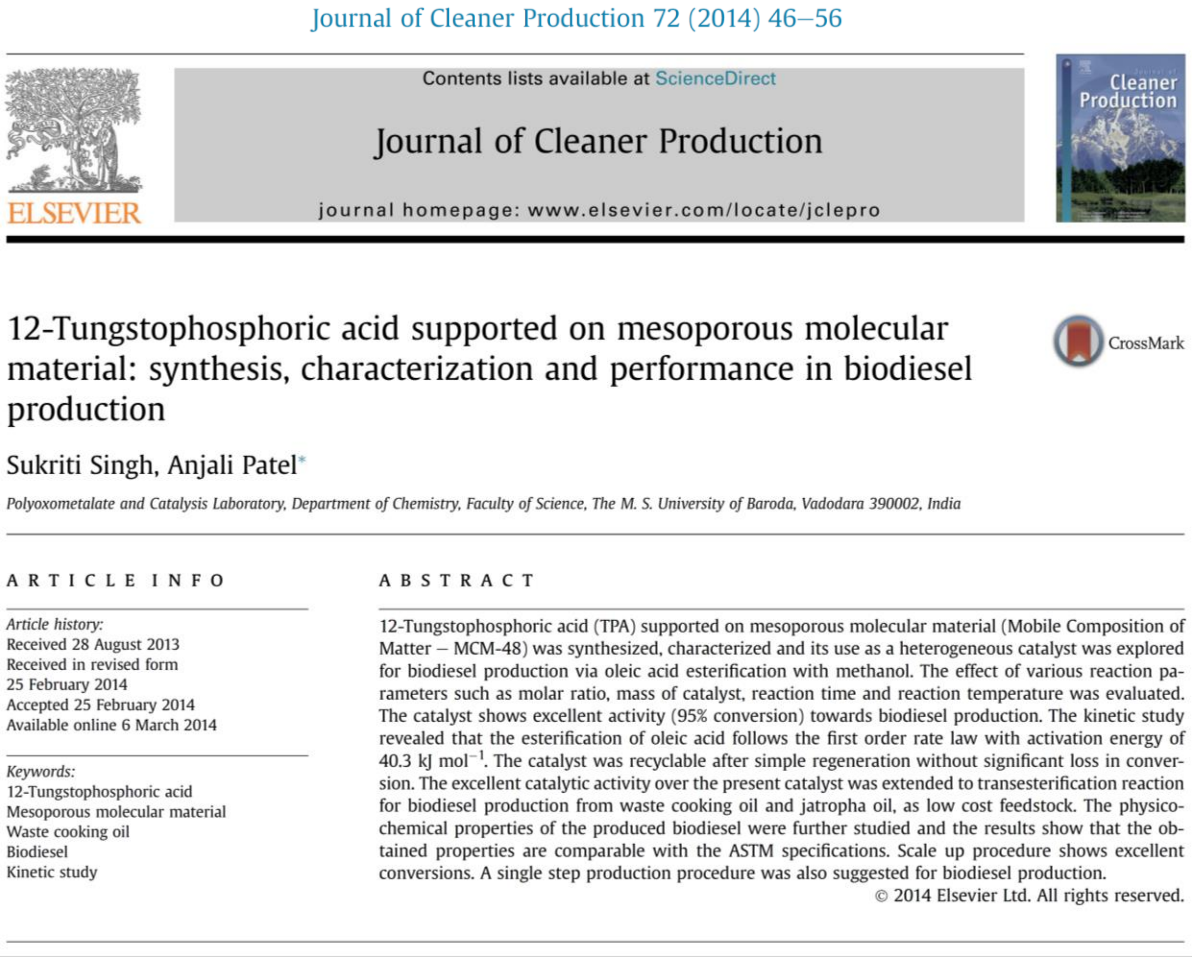

Journal of Cleaner Production 72 (2014) 46–56

Contents lists available at ScienceDirect

Journal of Cleaner Production

journal homepage: www.elsevier.com/locate/jclepro

12-Tungstophosphoric acid supported on mesoporous molecular material: synthesis, characterization and performance in biodiesel production

Sukriti Singh, Anjali Patel*

Polyoxometalate and Catalysis Laboratory, Department of Chemistry, Faculty of Science, The M. S. University of Baroda, Vadodara 390002, India

ARTICLE INFO

Article history:
Received 28 August 2013
Received in revised form
25 February 2014
Accepted 25 February 2014
Available online 6 March 2014

Keywords:
12-Tungstophosphoric acid
Mesoporous molecular material
Waste cooking oil
Biodiesel
Kinetic study

ABSTRACT

12-Tungstophosphoric acid (TPA) supported on mesoporous molecular material (Mobile Composition of Matter – MCM-48) was synthesized, characterized and its use as a heterogeneous catalyst was explored for biodiesel production via oleic acid esterification with methanol. The effect of various reaction parameters such as molar ratio, mass of catalyst, reaction time and reaction temperature was evaluated. The catalyst shows excellent activity (95% conversion) towards biodiesel production. The kinetic study revealed that the esterification of oleic acid follows the first order rate law with activation energy of 40.3 kJ mol^{-1}. The catalyst was recyclable after simple regeneration without significant loss in conversion. The excellent catalytic activity over the present catalyst was extended to transesterification reaction for biodiesel production from waste cooking oil and jatropha oil, as low cost feedstock. The physico-chemical properties of the produced biodiesel were further studied and the results show that the obtained properties are comparable with the ASTM specifications. Scale up procedure shows excellent conversions. A single step production procedure was also suggested for biodiesel production.

EXPERIMENTAL

Materials

All chemicals used were of A. R. grade. 12-Tungstophosphoric acid (PW_{12}), Disodium hydrogen phosphate (Na_2HPO_4), sodium tungstate dihydrate ($Na_2WO_4 \cdot 2H_2O$), acetone, ammonia, Ethanol, Cetyl triethyl ammonium bromide (CTAB) and Tetraethyl orthosilicate (TEOS) were used as received from Merck.

PW_{11} was synthesized by following the same method described in Chapter 1a.

Synthesis of MCM-48

The synthesis of MCM-48 was carried out as reported in literature [21]. Surfactant (CTAB, 2.4 g) was dissolved in 50 mL distilled water. To this, 50 mL ethanol (0.87 mol) and 12.6 mL of aqueous ammonia (32 wt%, 0.20 mol) were added. The mixture was stirred for 10 min. When the solution became homogeneous, 3.4 g of TEOS (16 mmol) was added. The molar composition of the gel was 1 M TEOS: 12.5 M NH_4OH: 54 M EtOH: 0.4 M CTAB: 174 M H_2O. After stirring for 2 h at room temperature, the resulting solid was filtered, washed with distilled water and dried in air at ambient temperature. The template was removed by calcination at 823 K for 6 h. The resulting material was designated as MCM-48. A schematic representation for synthesis of MCM-41 is shown in Figure 16.

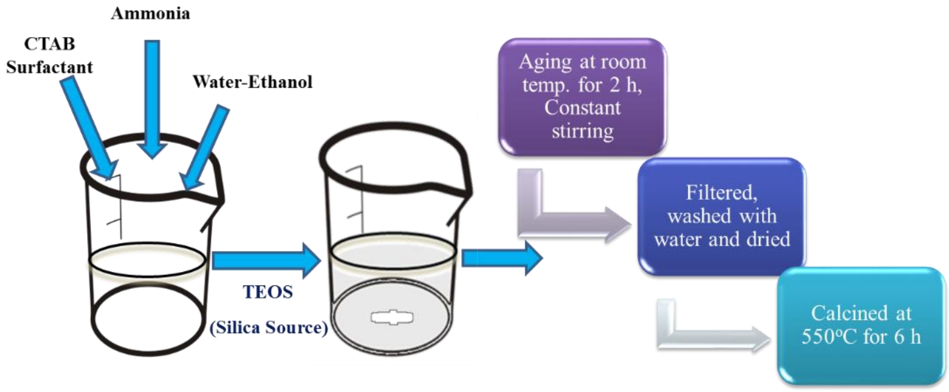

Figure 16. Synthesis scheme of MCM-48 under non-hydrothermal conditions.

Synthesis of the catalysts

PW_{12} anchored to MCM-48

PW_{12} was anchored to MCM-48 by impregnation method. 1 g of MCM-48 was impregnated with an aqueous solution of PW_{12} (0.1g/10 mL of distilled water). The water from the suspension was allowed to evaporate at 100 °C in an oven. Then the resulting mixture was dried at 100 °C with stirring for 10 h. The material thus obtained was designated as $(PW_{12})_1$/MCM-48. Same procedure was followed for the synthesis of a series of PW_{12} anchored catalyst (0.2-0.4 g/20-40 mL of distilled water). The obtained materials were designated as $(PW_{12})_2$/MCM-48, $(PW_{12})_3$/MCM-48 and $(PW_{12})_4$/MCM-48, respectively.

PW_{11} anchored to MCM-48

PW_{11} was anchored to MCM-48 by impregnation method. 1 g of MCM-48 was impregnated with an aqueous solution of PW_{11} (0.1 g/10 mL of distilled water). The water from the suspension was allowed to evaporate at 100 °C in an oven. Then the mixture was dried at 100 °C with stirring for 10 h. The obtained material was treated with 0.1 N HCl, filtered, washed with distilled water and dried at 100 °C. The material thus obtained was designated as $(PW_{11})_1$/MCM-48. Same procedure was followed for the synthesis of a series of PW_{11} anchored catalyst (0.2-0.4 g/20-40 mL of distilled water). The obtained materials were designated as $(PW_{11})_2$/MCM-48, $(PW_{11})_3$/MCM-48 and $(PW_{11})_4$/MCM-48, respectively. Leaching test was already shown in section 1a.

The **BET surface area**, pore diameter and pore volume of support as well as catalysts is presented in Table 5. As the loading of the active species (PW_{12}) increases, surface area decreases relative to the support. The decrease in total surface area of catalysts was due to incorporation of active species inside the mesopore channels of support and filling the pores as well as surface coverage. Similar trend was observed in the case of $(PW_{11})_3$/MCM-48. However, both surface area and pore diameter of $(PW_{11})_3$/MCM-48 are higher than those of $(PW_{12})_3$/MCM-48. This may be due to the fact that, removal of W-O unit from the parent PW_{12} results in decrease in the size of PW_{11} species leading to the increase in the available space inside the channels of the support. The decrease in surface area is first indication of chemical interaction between PW_{12}/PW_{11} with MCM-48. Further, up to 30% loading constant decrease in the surface area was observed which may be due to the monolayer formation of the active species. Further increase in loading up to 40% leads to the drastic decrease in the surface area as well as pore diameter (Table 5) due to blocking of the framework channels. Hence, 30% loaded catalysts were selected for the further detailed characterization.

Table 5. Textural properties of support and catalysts.

Materials	Surface area (m^2/g)	Pore diameter (Å)	Pore Volume (cm^3/g)
MCM-48	755	30.0	0.56
$(PW_{12})_1$/MCM-48	381	29.1	0.43
$(PW_{12})_2$/MCM-48	339	28.5	0.43
$(PW_{12})_3$/MCM-48	286	28.0	0.38
$(PW_{12})_4$/MCM-48	262	19.5	0.35
$(PW_{11})_1$/MCM-48	400	28.4	0.43
$(PW_{11})_2$/MCM-48	356	28.0	0.43
$(PW_{11})_3$/MCM-48	319	27.5	0.40
$(PW_{11})_4$/MCM-48	272	20.2	0.35

The N_2 adsorption-desorption isotherms of pure MCM-48, $(PW_{12})_3$/MCM-48 and $(PW_{11})_3$/MCM-48 (Figure 17) are of Type IV according to the IUPAC classification and exhibited a H1 hysteresis loop. A sharp increase in the isotherm between relative partial pressures 0.2 and 0.4 during adsorption and desorption indicates capillary condensation of N_2 in the mesopores, which is characteristic of mesoporous materials. Also, considerable adsorption amounts indicate that there is considerable volume of nanospaces even after the introduction of PW_{12}/PW_{11} species.

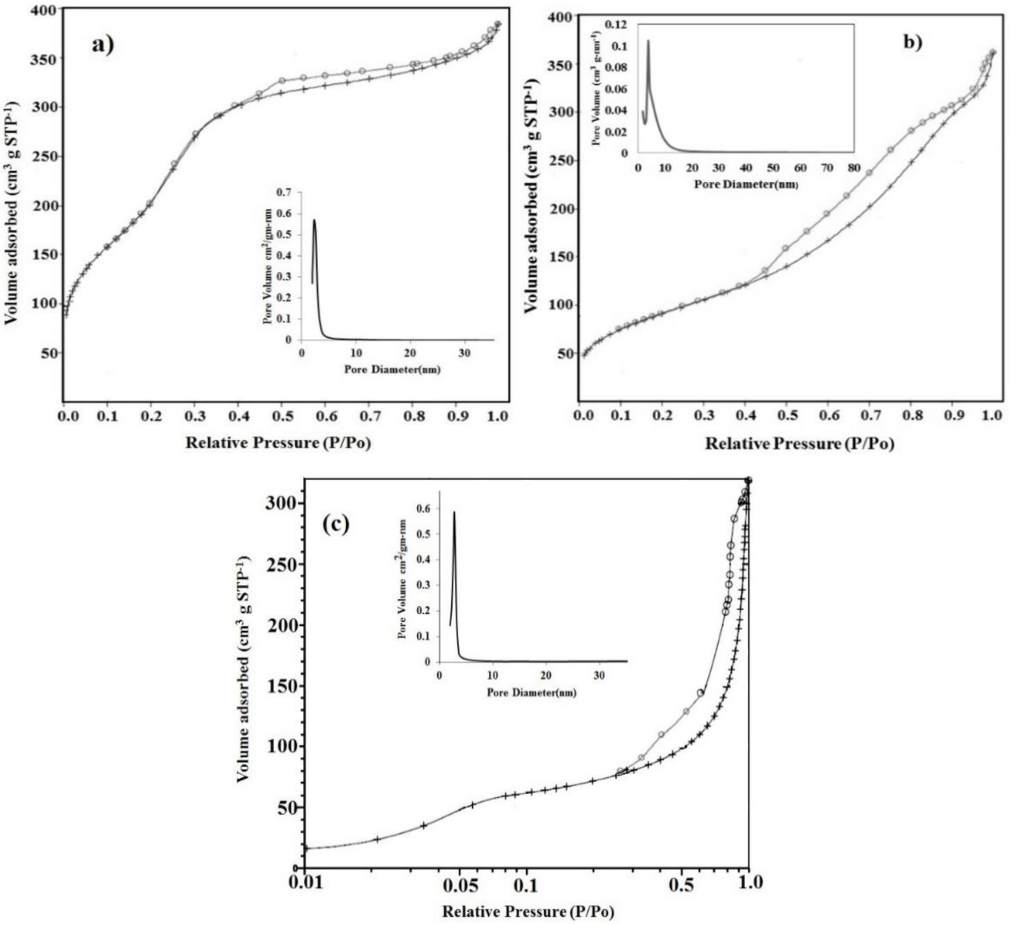

Figure 17. N_2 adsorption desorption isotherms of (a) MCM-48, (b) $(PW_{12})_3$/MCM-48 and (c) $(PW_{11})_3$/MCM-48.

The position of inflection point is related to the diameter of mesopores, and the sharpness of the step designates uniformity of mesopore size distribution. In addition, a narrow pore size distribution was observed for MCM-48, $(PW_{12})_3$/MCM-48 (Figure 17b) and $(PW_{11})_3$/MCM-48 (Figure 17c), indicating long range order over large scales. Slight broadening may be due to the introduction of active species inside the pores of MCM-48. The decrease in pore volume in catalyst is due to presence of PW_{12}/PW_{11} inside the channels of MCM-48.

The **EDS elemental analysis** for $(PW_{12})_3$/MCM-48 and $(PW_{11})_3$/MCM-48 is shown in Table 6. The results obtained from EDS were in good agreement with the analytically calculated values.

Table 6. EDS elemental analysis.

Catalyst	Elemental analysis (weight %)					
	O	Si	W		P	
			By EDS	Theoretical	By EDS	Theoretical
$(PW_{12})_3$/MCM-48	54.6	27.9	17.2	17.7	0.30	0.32
$(PW_{11})_3$/MCM-48	54.1	29.8	15.9	16.5	0.18	0.19

TG-DTA analysis of the support and the catalyst was carried out (Figure 18). MCM-48 shows initial weight loss of 8.4% up to 150 ^oC (Figure 18a). This was further accompanied by a broad band on the DTA curve, appearing as an endothermic peak at 80 ^oC. This initial weight loss may be due to desorption of physically adsorbed water molecules. The final 3.22% weight loss above 450 ^oC may be due to the condensation of silanol groups to form siloxane bonds. After that, absence of any weight loss indicates that support is stable up to 550 ^oC. The TG-DTA of $(PW_{12})_3$/MCM-48 (Figure 18b) shows initial weight loss of 10-13% up to 150 ^oC, due to loss of adsorbed water. Second weight loss of 1-2% between 200 and 350 ^oC corresponds to the loss of water of crystallization of Keggin ion. A gradual weight loss from 350 to 500 ^oC was observed due to the difficulty in removal of water present in PW_{12} molecules inside the channels of MCM-48. This type of inclusion can cause the stabilization of PW_{12} molecules inside the channels of MCM-48. As compared to pure PW_{12}, absence of any endothermic peak in DTA curve at 485 ^oC indicates that the stability of PW_{12} increases up to 550 ^oC after supporting on MCM-48.

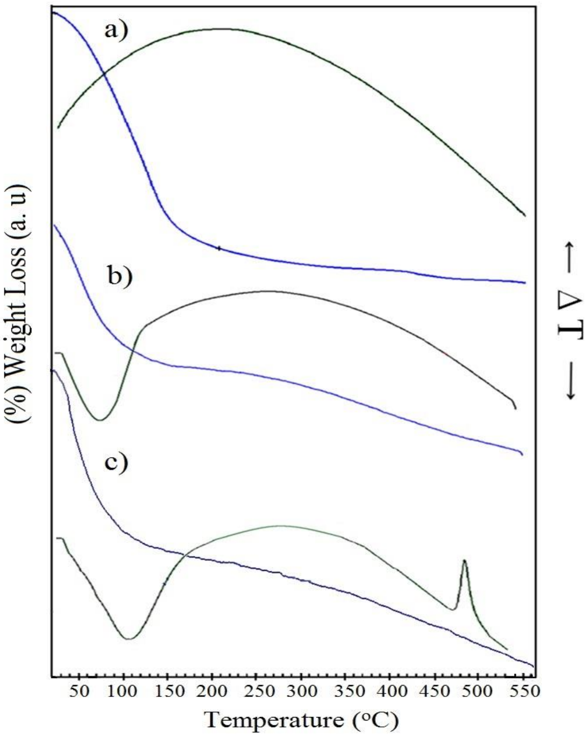

Figure 18. TG-DTA of (a) MCM-48, (b) $(PW_{12})_3$/MCM-48 and (c) $(PW_{11})_3$/MCM-48.

The TGA of $(PW_{11})_3$/MCM-48 (Figure 18c) shows first weight loss of 7% up to 150 °C, due to removal of adsorbed water. Second weight loss of 12% between 200 to 350 °C corresponds to the loss of water of crystallization from lacunary anion. A gradual weight loss of 7% in the range 350 to 550 °C was due to difficulty in removal of water (present in PW_{11} inside the channels of MCM-48). This type of inclusion results in stabilization of PW_{11} molecules inside MCM-48 channels.

FT-IR spectrum of MCM-48 shows a broad band around 1100 and 1165 cm^{-1} corresponding to asymmetric stretching of Si-O-Si (Figure 19b). The bands at 640 and 458 cm^{-1} are due to symmetric vibrations of Si-O-Si and bending vibrations of Si-O, respectively. The broad band at 3448 cm^{-1} is due to the absorption of O-H from large amount of H_2O hydrogen bonded to Si-OH, which provides opportunities for forming hydrogen bonds. The obtained bands are in good agreement with the reported literature [22].

The typical bands for PW_{12} at 982 cm^{-1} corresponds to v_{as} vibration of $W=O_d$ (terminal oxygen linked to a lone tungsten atom), and 897 cm^{-1} for stretching vibrations of $W-O_b-W$ (corner sharing oxygen's of two different triads of tungsten atom) are clearly observed in $(PW_{12})_3$/MCM-48 (Figure 19c). Appearance of these fingerprint bands strongly indicate that the primary structure of PW_{12} is completely retained even after impregnation on the support. The absence of vibration band at 1080 cm^{-1} (V_s stretching of P-O) in PW_{12} may be due to superimposition with the bands of MCM-48. FT-IR spectra of $(PW_{12})_3$/MCM-48 also show the peaks at 1637 and 3450 cm^{-1} with a shoulder at 3250 cm^{-1}. This probably corresponds to the bending and stretching vibrations of bridging hydroxyl, which may be due to the interaction of PW_{12} anions and hydrogen of silanol groups of MCM-48.

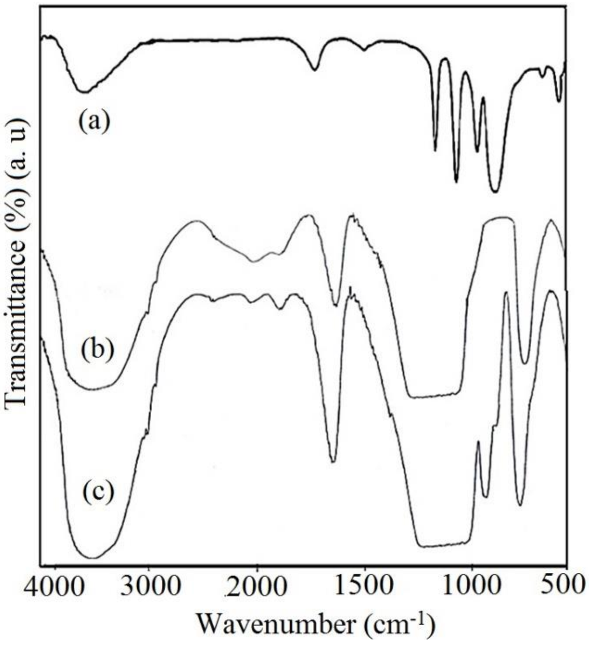

Figure 19. FT-IR spectra of (a) PW_{12}, (b) MCM-48 and (c) $(PW_{12})_3$/MCM-48.

The FT-IR spectrum of PW_{11} has been explained in ***Chapter 1a***. The FT-IR spectrum of $(PW_{11})_3$/MCM-48 (Figure 20b) shows bands at 957 cm^{-1} and 875 cm^{-1} assigned to W=O and W-O-W stretches, respectively. The shift in bands indicate a strong hydrogen bonding interaction between silanol groups of the support and PW_{11}.

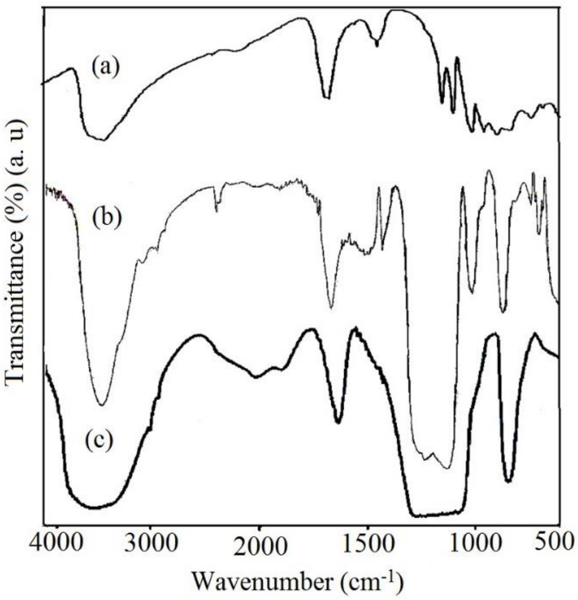

Figure 20. FT-IR spectra of (a) PW_{11}, (b) $(PW_{11})_3$/MCM-48 and (c) MCM-48.

Raman spectrum of PW_{12} (Figure 21a) shows bands at 1010, 990, 900, 550, and 217 cm^{-1}, which have been assigned to v_s (W-O $_d$), v_{as} (W-O $_d$), v_{as} (W-O_b-W), v_s (W-O $_c$-W), and v_s (W-O $_a$), respectively [11] as discussed in *part 1a*. For $(PW_{12})_3$/MCM-48 (Figure 21b) the presence of all the bands of PW_{12}, without any significant shift indicates the retainment of Keggin unit even after supporting. However, slight lowering in intensity was observed, which might be due to the interaction with support.

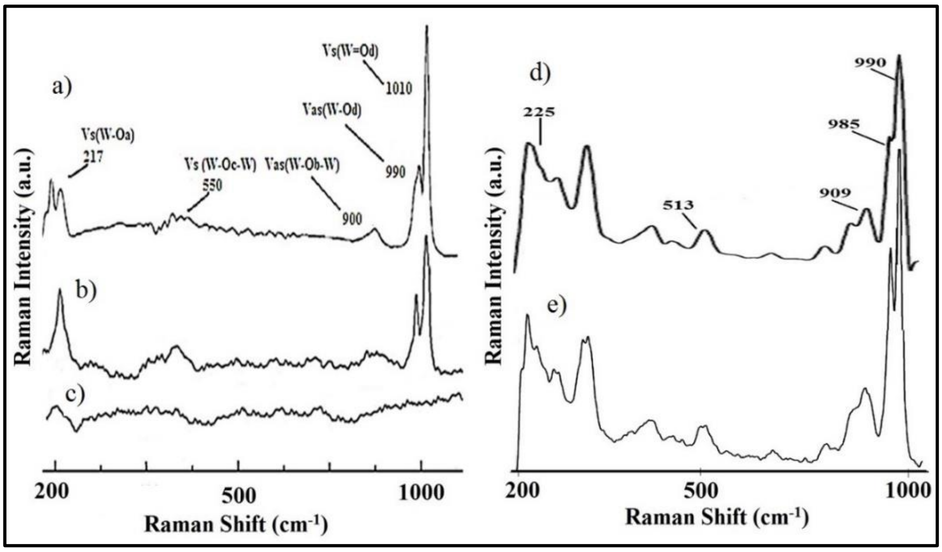

Figure 21. FT-Raman spectra of (a) PW_{12}, (b) $(PW_{12})_3$/MCM-48, (c) MCM-48, (d) PW_{11} and (e) $(PW_{11})_3$/MCM-48.

Raman spectrum of PW_{11} (Figure 21d) show bands at 990, 985, 909, 513, and 225 cm-1, corresponding to ν_s (W=O_d), ν_{as} (W-O_d), ν_{as} (W-O_b-W), ν_s (W-O_c-W), and ν_s (W-O_a), respectively [23], as discussed in *part 1a.* The spectrum of $(PW_{11})_3$/MCM-48 (Figure 21e) displays all the bands for PW_{11} confirming the retention of the structure. Presence of all reported bands of lacunary PW_{11} in catalyst indicates that the structure of PW_{11} is intact even after anchoring.

^{31}P MAS NMR spectra of PW_{12} and $(PW_{12})_3$/MCM-48 are shown in Figure 22. PW_{12} shows a single peak at -15.62 ppm (Figure 22a) and is in good agreement with the reported one [16]. It has been reported by Mizuno and Misono, that crystalline PW_{12} is more thermally stable and most of the crystallites become partially dehydrated during thermal treatment. As a result, the chemical shift are in the range -11.2 to -15.2 ppm [24, 25]. Further, they have also reported that the dispersion as well as interaction with the support can be correlated with the NMR results. The observed shift in $(PW_{12})_3$/MCM-48, at -12.03 ppm can be correlated with the above discussion (Figure 22b) and value can be assigned to partially dehydrated intact Keggin structure of PW_{12} which is highly dispersed inside the three dimensional structure of MCM-48 [26, 27] by strong interaction with the support (in the present case, due to the formation of the species $[(Si\text{-}OH_2^+)_2(HPW_{12}O_{40})_2]$ [17].

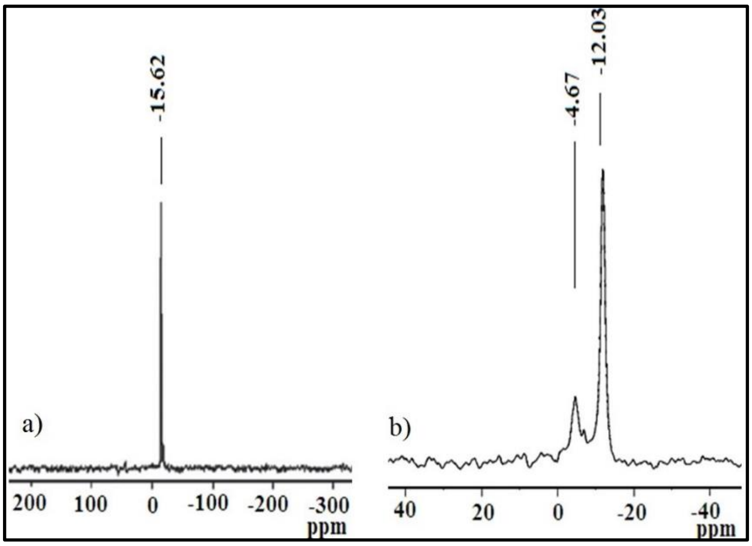

Figure 22. ^{31}P MAS NMR spectra (a) PW_{12} and (b) $(PW_{12})_3$/MCM-48.

However, shift from -15.6 to -12.03 ppm is due to the strong interaction with the support as explained above. An additional, very low intensity peak at -4.6 ppm is due to adsorbed phosphorous species derived from the highly fragmented Keggin species. This observation agrees well with the related values reported by Edwards et al. [17]. Absence of any chemical shift around -10 ppm confirms that there is no decomposition of the Keggin unit [28].

^{31}P MAS NMR spectrum of PW_{11} (Figure 23a) shows a peak at -11.3 ppm corresponding to formation of mono lacunary species. The spectrum for $(PW_{11})_3$/MCM-48 (Figure 23b) reveals two resonances: at -10.5 ppm which may be due to the presence of strongly adsorbed highly fragmented Keggin unit and an intense peak at -11.8 ppm due to intact PW_{11} anion interacting with surface hydroxyl groups of support. These observations are well in agreement with the related values reported by Edwards et al. [17] which indicates that the active species-PW_{11} is present in the fragmented form, but not decomposed.

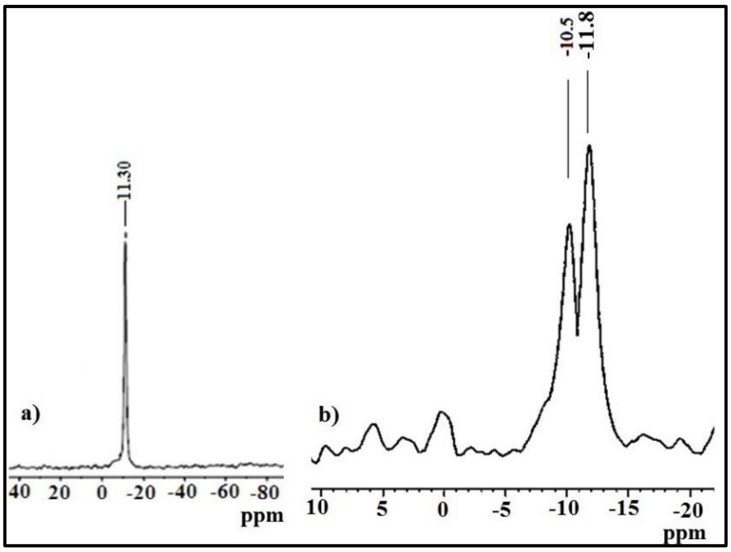

Figure 23. ^{31}P MAS NMR spectra (a) PW_{11} and (b) $(PW_{11})_3$/MCM-48.

A slight broadening and shifting in the peak may be due to interaction of PW_{11} with the silanol (-OH) groups of MCM-48. Based on the above results, we concluded that the structure of lacunary anion remains intact after formation of the catalyst.

^{29}Si MAS-NMR spectra of MCM-48 and $(PW_{12})_3$/MCM-48 can be seen in Figure 24. A broad peak for MCM-48 between -90 and -125 ppm was observed, attributed to three main components with chemical shifts at -96, -102.3, and -110.5 ppm [29]. For MCM-48 (Figure 24a, Table 7) the signals resulted from Q^2 (-96 ppm), Q^3 (-102.3 ppm), and Q^4 (-110.5 ppm) silicon nuclei, where Q^x corresponds to a silicon nuclei with x siloxane linkages, i.e., Q^2 to disilanol Si-(O- Si)$_2$(-O-X), where X is H or PW_{12}/PW_{11}, Q^3 to silanol (X-O)-Si-(O-Si)$_3$, and Q^4 to Si-(O-Si)$_4$ in the framework. The observed values of chemical shifts for MCM-48 are in good agreement with the reported literature.

The spectrum of $(PW_{12})_3$/MCM-48 (Figure 24b) shows slight shift in the chemical shift values (Table 7) and the peaks were relatively broad as compared to MCM-48, which may be due to the presence of PW_{12}. Also the intensity of Q^2 and Q^3 peaks decreases on loading PW_{12} on the support (MCM-48). The decrease in intensity of Q^2 and Q^3 peaks was an indication of bonding of silanol groups with PW_{12} inside the pores of MCM-48. This indicates that the mesoporous structure of MCM-48 is not disturbed due to the presence of PW_{12} and there is a strong interaction of PW_{12} with the support.

Table 7. ^{29}Si chemical shifts of support and catalyst.

Material	Q^2 ppm	Q^3 ppm	Q^4 ppm
MCM-48	-96.0	-102.3	-110.5
$(PW_{12})_3$/MCM-48	-99.0	-102.0	-110.0
$(PW_{11})_3$/MCM-48	-99.0	-101.3	-110.3

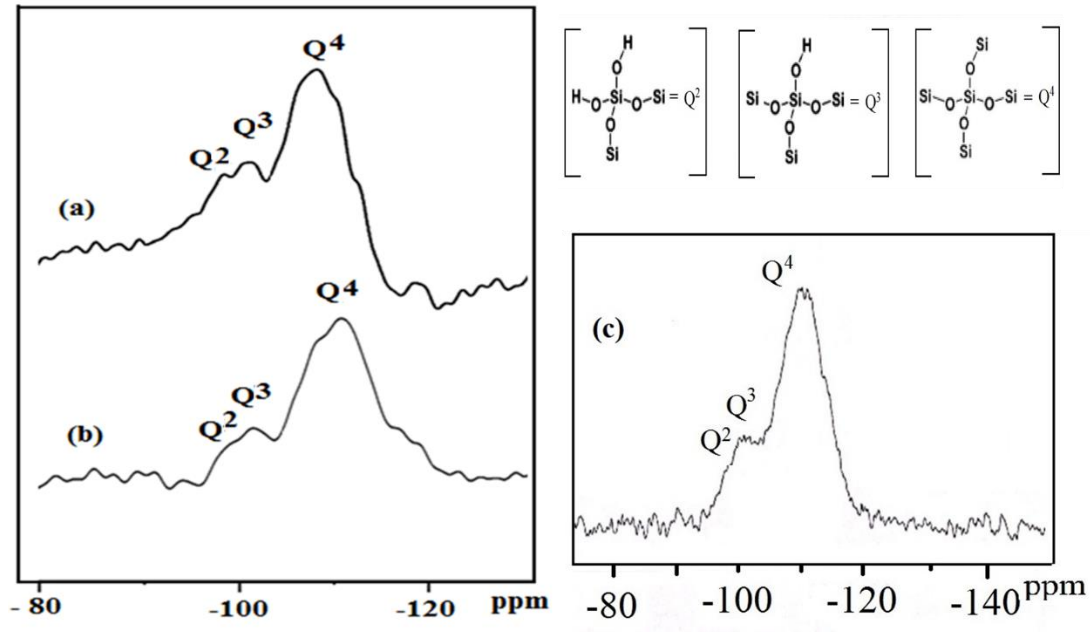

Figure 24. ^{29}Si MAS NMR spectra of (a) MCM-48, (b) $(PW_{12})_3$/MCM-48 and (c) $(PW_{11})_3$/MCM-48.

Establishment of chemical interaction between PW_{11} and MCM-48 was also confirmed by ^{29}Si MAS NMR (Figure 24c). The spectrum of $(PW_{11})_3$/MCM-48 (Figure 24c) shows three characteristic peaks with slight change in chemical shifts values at -99 (Q^2), -101.3 (Q^3), and -110.3 ppm (Q^4) (Table 7). The catalyst shows relatively broad peaks as compared to MCM-48, which may be due to the presence of PW_{11}. The Q^4 peak was not disturbed, indicating retention of mesoporous structure of the support even after incorporation of PW_{11}. Also the observed decrease in intensity of Q^2 and Q^3 peaks in catalyst was an indication of chemical/bonding interaction between the silanol groups of MCM-48 with PW_{11}.

The **low angle XRD** pattern of MCM-48 (Figure 25) displays key characteristic peaks at 2.3^{o} and in addition a broad shoulder at 3.0 ^{o} corresponding to plane (211) and (220), respectively was also observed. Some peaks in range 4-5^{o} corresponds to the reflections of (400), (321) and (420) planes of MCM-48 mesostructure with *Ia*3*d* cubic symmetry [30].

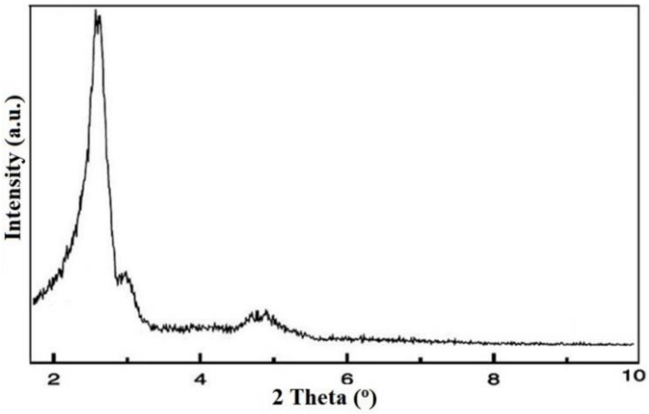

Figure 25. Low angle powder XRD pattern of MCM-48.

Full range XRD pattern of $(PW_{12})_3$/MCM-48 (Figure 26c, Left) shows absence of any characteristic peaks of the crystalline phase of PW_{12} indicating fine dispersion of PW_{12} inside the pores of MCM-48. Further, the mesoporous structure of MCM-48 is rather intact even after introduction of PW_{12}. Slight broadening and decrease in the intensity of the main peak was observed in the catalyst which was in good agreement with the report by Sakthivel et al. [31].

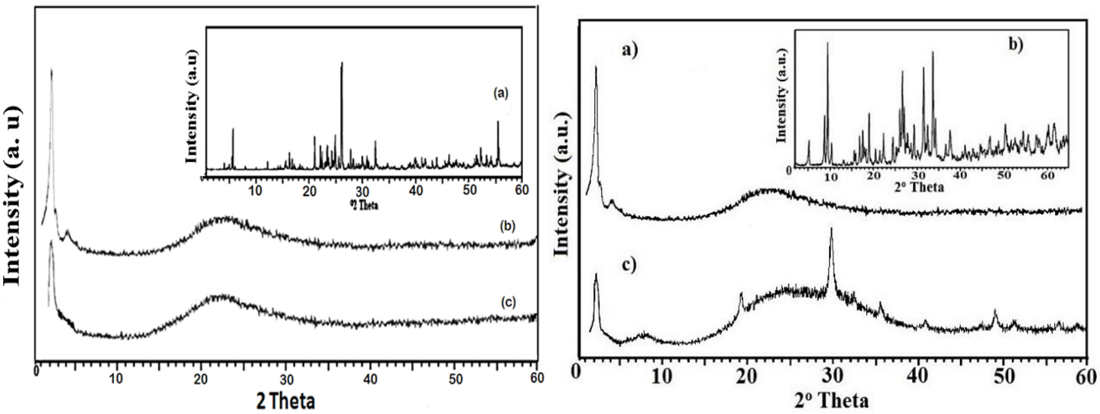

Figure 26. X-ray diffraction patterns, Left- (a) PW_{12}, (b) MCM-48 and (c) $(PW_{12})_3$/MCM-48; Right- (a) MCM-48, (b) PW_{11} and (c) $(PW_{11})_3$/MCM-48.

XRD pattern of $(PW_{11})_3$/MCM-48 (Figure 26c, Right) shows appearance of main characteristic peaks of MCM-48, however, the intensities of diffraction peaks decrease on loading PW_{11}. This can be due to the fact that introducing the guest species may reduce the scattering contrast between pore walls and pore spaces. Slight broadening and shift in main peak of MCM-48 at 2.3° was observed [31], which is attributed to the tunnel sizes, increase of lattice defects and their interaction with MCM-48 framework. Also in the catalyst, very small low intensity peaks for PW_{11} appear, however, not all the typical characteristic diffraction peaks of PW_{11} can be observed. Absence of any aggregates of PW_{11} indicates fine dispersion inside the mesopores of MCM-48, since the pore size of MCM-48 is larger than that of PW_{11}. Hence, XRD confirms retention of mesoporous structure of MCM-48 even after introduction of PW_{12}/PW_{11}.

SEM image of MCM-48 (Figure 27a) demonstrates fine, spherical particles of uniform diameter and particle size. SEM image of $(PW_{12})_3$/MCM-48 (Figure 27b) and $(PW_{11})_3$/MCM-48 (Figure 27c) depicts that the catalysts have homogeneous distribution of spherical particles and the structure is not affected upon introduction of PW_{12}/PW_{11}. Further, no change in surface morphology and absence of separate crystallites of bulk phase, PW_{12}/PW_{11}, in the catalyst indicates that PW_{12}/PW_{11} species are well dispersed inside the 3D pores of the support, which goes well with the surface area and XRD data.

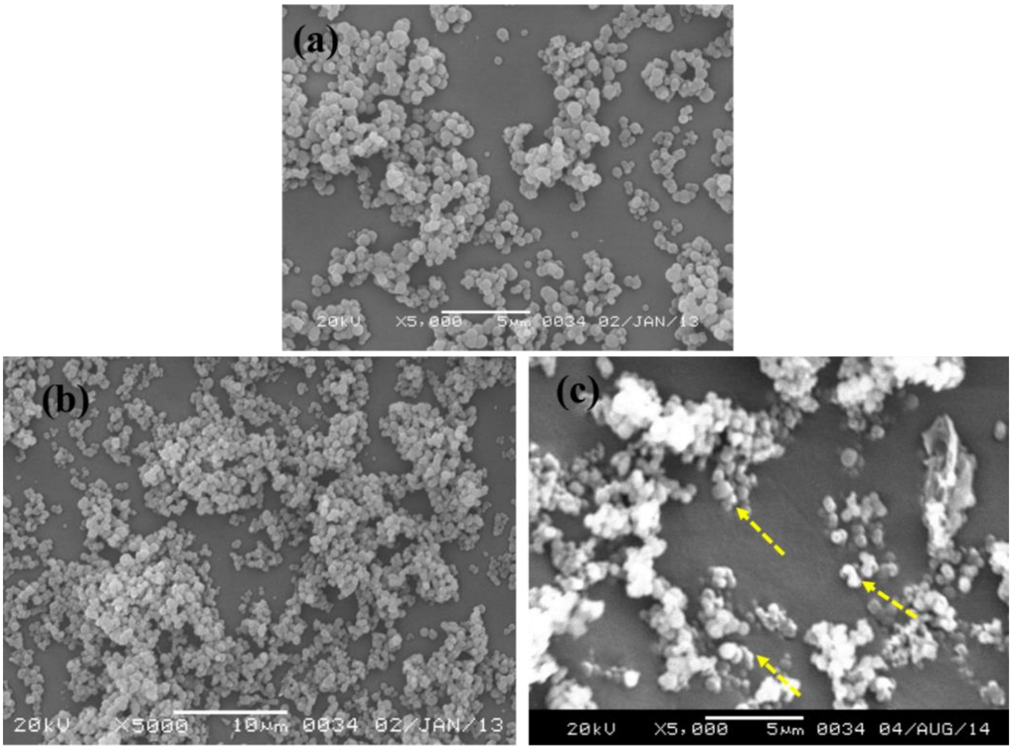

Figure 27. SEM micrographs of (a) MCM-48, (b) $(PW_{12})_3$/MCM-48 and (c) $(PW_{11})_3$/MCM-48.

TEM images of MCM-48 shows very well ordered pore system with pore diameter between 2.5 and 4 nm (Figure 28a, b). It is well known in literature, that MCM-48 has 3D pore system with two non-intersecting gyroidal pores which can assist dispersion of material having diameter in the range 1-3 nm. $(PW_{12})_3$/MCM-48 (Figure 28c, d) show ordered 3D channels that are well arranged over a large scale. Furthermore, the absence of characteristic peaks of the crystalline phase of PW_{12} in the catalyst indicates that PW_{12} is highly dispersed inside the channels of MCM-48.

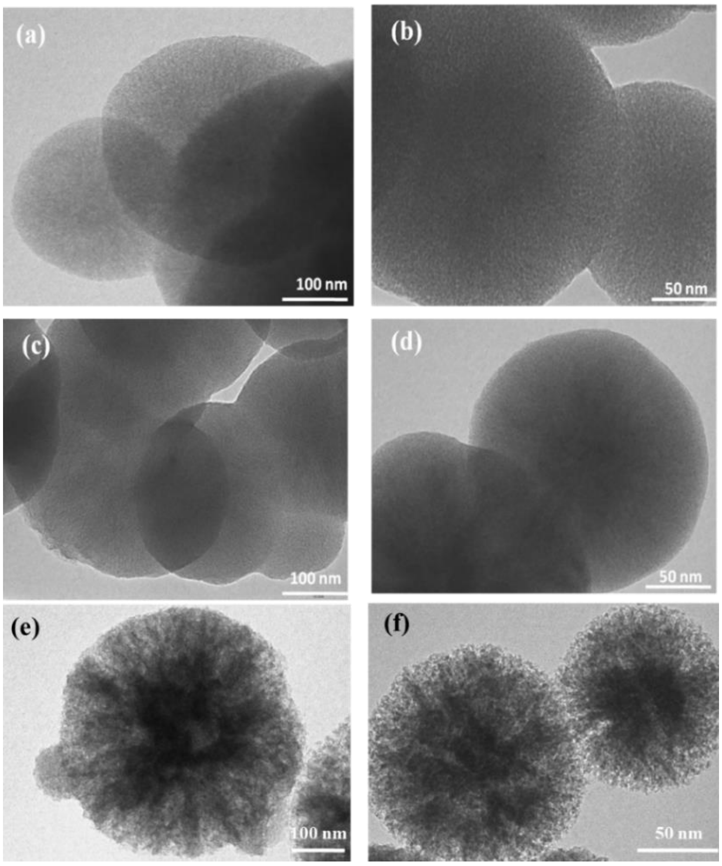

Figure 28. TEM images of (a, b) MCM-48; (c, d) $(PW_{12})_3$/MCM-48; and (e, f) $(PW_{11})_3$/MCM-48.

TEM image of $(PW_{11})_3$/MCM-48 (Figure 28 e, f) also shows well-ordered hexagonal nano-channels on a large scale. The morphology of catalyst was almost same as compared to MCM-48, indicating no bigger agglomerated PW_{11} particles and the pore system seems to be similar upon impregnation procedure.

Acidity was measured by **potentiometric titration** and the plot of potential as a function of meq. n-butylamine/g of support or catalysts is shown in Figure 29. It was observed that as PW_{12}/PW_{11} loading increases, total acidity also increases as the variation in number of acidic sites is dependent on the amount of PW_{12}/PW_{11} present in the catalyst (Table 8). The potentiometric curves for 30% loading catalysts showed initial potential- 450 mV $(PW_{12})_3$/MCM-48 and 290 mV $(PW_{11})_3$/MCM-48, corresponding to very strong acidic sites arising due to strong acidic nature of phosphotungstates.

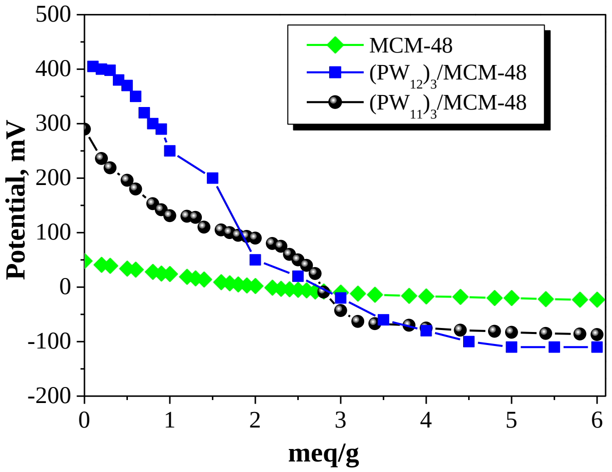

Figure 29. Potentiometric titration curves of support and catalysts.

It is also interesting to note that all values, especially a drastic decrease in the acidic strength of $(PW_{11})_3$/MCM-48 as compared to $(PW_{12})_3$/MCM-48 (Table 8). The reason being, the acidic character of polyoxometalates is mainly due to the acidic addenda atoms i.e. tungsten in the present case and removal of one tungsten-oxygen unit from the parent PW_{12} is expected to decrease the acidity of the PW_{11}. The obtained value is in good agreement with the expected one.

Table 8. Potentiometric n-butylamine acidity of support and the catalysts.

Catalyst	Acidic Strength Ei (mV)	Strength of acid sites (mequiv. g^{-1})		No. of acid sites (mequiv. g^{-1})
		Very strong	Strong	
MCM-48	60	0	2.2	2.2
$(PW_{12})_3$/MCM-48	450	1.8	2.0	3.9
$(PW_{11})_3$/MCM-48	290	1.2	2.1	3.4

Conclusions

- Synthesis of sodium salt of PW_{11} was achieved successfully, and confirmed by *elemental* and *spectral* studies.
- MCM-41 and MCM-48 were synthesized by *non-hydrothermal synthetic method*, and catalysts were prepared by anchoring PW_{12}/PW_{11} to these supports.
- *Thermal stability* of PW_{12}/PW_{11} increases after *anchoring* and catalysts were stable up to ~485 °C.
- FT-IR and Raman spectra show that *Keggin ion structure* of PW_{12}/PW_{11} *remains intact* even after anchoring to MCM-41/MCM-48.
- BET surface area, ^{31}P MAS NMR, ^{29}Si MAS NMR data and Raman studies show that there is a *strong interaction*, hydrogen bonding, between surface oxygens of PW_{12}/PW_{11} with the silanol groups of MCM-41/MCM-48. From *spectroscopic characterization*, the possible interaction between the support and PW_{12}/PW_{11} is as follows,

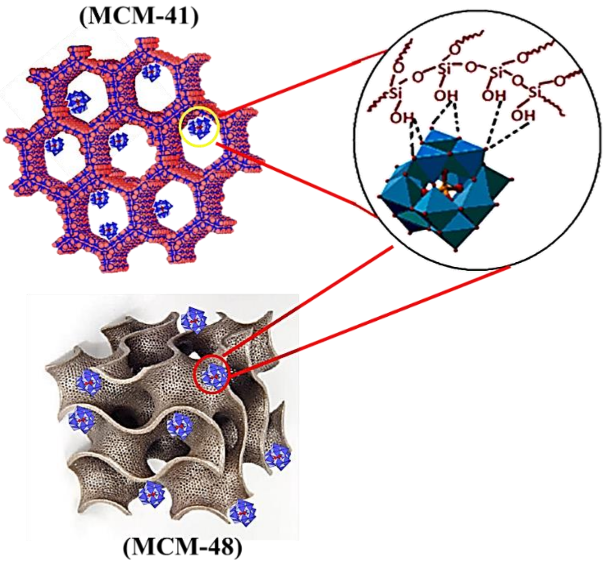

- Low angle powder XRD, SEM and TEM confirms uniform dispersion of PW_{12}/PW_{11} inside the *hexagonal* or *three dimensional channels* of MCM-41/MCM-48, respectively.

References

1. C. Brevard, R. Schimpf, G. Tourne, C. M. Tourne, J. Am. Chem. Soc., 105, 7059, (1983).
2. Q. Cai, Z. S. Luo, W. Q. Pang, Y. W Fan, X. H. Chen, F. Z. Cui, Chem. Mater. 13, 258, (2001).
3. V. Brahmkhatri, A. Patel, Ind. Eng. Chem. Res., 50, 6620, (2011).
4. J. M. Thomas, W. J. Thomas, *Principles and Practice of Heterogeneous Catalysis*, VCH, Weinheim, (1997).
5. R. A. van Santen, P. W. N. M. Van Leeuwen, J. A. Moulijin, B. A. Averil (Eds.), *Catalysis: An Integrated Approach*, Elsevier, Amsterdam, 2nd ed., (1999).
6. R. Richards (Eds.), *Surface and Nanomolecular Catalysis*, CRC press, Chapter-1, Pg-2, (2006).
7. J. L. G. Fierro, *Spectroscopic Characterization of Heterogeneous Catalysts*, Stud. Surf. Sci. Cat., Elsevier, vol. 57A, (1990).
8. P. Ferreira, I. M. Fonseca, A. M. Ramos, J. Vital, J. E. Castanheiro, Appl. Catal. B: Env., 98, 94, (2010).
9. A. Vogel, *A Textbook of Quantitative Inorganic Analysis*, 2nd ed., Longman, Green and Co., London, Pg- 491, (1951).
10. C. Brevard, R. Schimpf, G. Tourne, C. M. Tourne, J. Am. Chem. Soc., 105, 7059, (1983).
11. B. Li, W. Ma, J. Liu, S. Zuo, X. Li, J. Colloid Interface Sci., 362, 42, (2012).
12. R. Massart, R. Contant, M. Fruchart, P. Ciabrini, M. Fournier, Inorg. Chem., 16, 2916, (1977).
13. G. D. Yadav, V. V. Bokade, Appl. Catal. A: Gen., 147, 299, (1996).
14. Y. Luo, Z. Hou, R. Li, X. Zheng, Microporous Mesoporous Mater., 109, 585, (2008).
15. C. Rocchiccioli- Deltcheff, Inorg. Chem., 22, 207, (1983).
16. T. Okuhara, N. Mizuno, M. Misono, Adv. Catal., 41, 113, (1996).
17. J. Edwards, C. Thiel, B. Benac, J. Knifton, Catal. Lett., 51, 77, (1998).

18. X. S. Zhao, G. Q. Lu, A. K. Whittaker, G. J. Millar, H. Y. Zhu, J. Phys. Chem.: B., 101, 6525, (1997).
19. A. E. Rahman, S. Khdera, H. M.A. Hassana, M. S. El-Shall, Appl. Catal A: Gen., 411-412, 77, (2012).
20. P. Vazquez, L. Pizzio, C. Caceres, M. Blanco, H. Thomas, E. Alesso, L. Finkielsztei, L. Lantano, G. Moltrasio, J. Aguirre, J. Mol. Catal. A: Chem., 161, 223, (2000).
21. D. Kumar, K. Schumacher, C.D.F.V. Hohenesche, M. Grun, K.K. Unger, Colloid Surf. A: Physicochem. Eng. Asp., 187-188, 109, (2001).
22. Z. Yijun, Y. Shuijin, J. Wuhan Univ. Technol. Mater. Sci. Ed., 23, 346, (2008).
23. Z. E. A. Abdalla, B. Li, Chem. Eng. J., 200-202, 113, (2012).
24. N. Mizuno, M. Misono, Chem. Lett., 16, 967, (1987).
25. M. Misono, Chem. Commun., 1141, (2001).
26. B. M. Devassy, S. B. Halligudi, S. G. Hegde, A. B. Halgeri, F. Lefebvre, Chem. Commun., 1074, (2002).
27. B. M. Devassy, F. Lefebvre, S. B. Halligudi, J. Catal., 231, 1, (2005).
28. T. H. Chang, J. Chem. Soc. Faraday Trans., 91, 375, (1995).
29. H. Gies, S. Grabowski, M. Bandyopadhyay, W. Grunert, O. P. Tkachenko, K. V. Klementiev, A. Birkner, Microporous Mesoporous Mater., 60, 31, (2003).
30. J. Xu, Z. Luan, H. He, W. Zhou, L. Kevan, Chem. Mater., 10, 3690, (1998).
31. A. Sakthivel, K. Komura, Y. Sugi, Ind. Eng. Chem. Res., 47, 2538, (2008).